NTNU

Norwegian University of
Science and Technology

Two-dimensional Simulations of Particle Deposition on a Cylinder in a Turbulent Cross Flow at Intermediate Reynolds Numbers

Nikolai Hydle Rivedal

Master of Science in Physics and Mathematics
Submission date: June 2011
Supervisor: Jon Andreas Støvneng, IFY
Co-supervisor: Nils Erland Haugen, SINTEF Energi

Norwegian University of Science and Technology
Department of Physics

NTNU
Department of Physics

Two-dimensional Simulations of Particle Deposition on a Cylinder in a Turbulent Cross Flow at Intermediate Reynolds Numbers

Master's Thesis

Nikolai Hydle Rivedal
Supervisor: Nils Erland L. Haugen

June 2011

Abstract

The behaviour of particles in turbulent flow, with emphasis on particle deposition on both the frontside and backside of a cylinder, was investigated by means of Direct Numerical Simulations. One-way coupling between fluid and particles was applied. Simulations of turbulence forced at small, intermediate and large scales were run on a three-dimensional domain. The turbulence was used as inlet on a two-dimensional flow domain, where a Lagrangian tracker was used to compute the particle motions.

The Reynolds numbers used were $\mathrm{Re_c} = 421$ and $\mathrm{Re_c} = 1685$. For intermediate Stokes numbers, or particle sizes, the number of particles deposited increased when the Reynolds number was raised. The presence of turbulence lead to a further increase in the deposition for these Stokes numbers, compared to the deposition in laminar flow. The increase was at its highest for large scale forced turbulence. The increased deposition of particles of intermediate Stokes numbers on the frontside of the cylinder in turbulent flow was found to be related to the variance of the effective Stokes number, resulting from the fluctuating nature of the turbulent velocity. The deposition of particles with small Stokes numbers was also altered by the presence of turbulence, but this could not be explained by the variance of Stokes number. The mechanism leading to deposition of these smallest particles is related to the turbulent eddies close to the boundary layer of the cylinder, and will need further study.

At the backside of the cylinder, the increased deposition at raised Reynolds number and at the presence of turbulence was related to the magnitude of vorticity. Furthermore, preferential concentration of particles in turbulence was observed in the $\mathrm{Re_c} = 1685$ cases, demonstrating the effect of the vorticity magnitude being sustained throughout the domain.

Preface

This thesis is the finishing work of my Master's Degree in Applied Physics and Mathematics. The work was done at SINTEF Energy Research in collaboration with Department of Physics at NTNU. I chose Computational Fluid Dynamics as a field of specialization because of its vast possibilities and applications in the world of applied physics. And as a bonus, it is fun! I also consider SINTEF Energy Research to play a significant role in prospective energy scenarios in our society, and am glad I have had the opportunity to write my thesis there.

The present work is a continuation of the specialization project I did in the fall of 2010. In addition to going further from where the project report ended, this thesis contains relevant results from that work.

Acknowledgements

First of all, I am grateful to my very supportive supervisor Nils Erland L. Haugen. He has been brilliant whenever we have faced challenges, and patient when it has come to my poor Linux skills. Also, with Jon Andreas Støvneng as my formal supervisor at Department of Physics, I knew I was in good hands. I am thankful to Jens Jensen, for great moments at the office. Furthermore, I want to thank Vebjørn Tveiterås for being the most critical person I know, in a nice way. His comments were of invaluable help for improving the text. Kristoffer Hellton also did an excellent job with detecting errors and coming up with suggestions for improvement. Erik Løkken Walter deserves a big thanks for lending me a laptop when my own laptop monitor all of a sudden went black and everything seemed literally dark.

And most importantly, thanks to Marita for being so caring and lovable, every single day and night.

Nikolai Hydle Rivedal,
June 30, 2011

Contents

List of Figures

List of Tables

Chapter 1

Introduction

1.1 Background and motivation

Particle-laden flows are of significant importance in various fields in engineering and technology as well as natural and environmental processes. It may be transport of sediments in rivers or the deposition of small particles in the human lung. More specifically, particles in a gas flow can be seen in many everyday settings, being for example dust carried by air and deposited on surfaces of solids. Among other applications and fields of research where the knowledge of particle-laden flows is crucial, Boivin et al. (1998) [1] mention the combustion of pulverized coal, or liquid sprays, gas-phase reactions controlled by particulate catalysts, dust storms and the dispersal of pollutants in the atmosphere. In short, the areas of interest are many and diverse.

Filters are found in mechanic and electronic devices, where particles of different origins may settle, or *deposit*. The filters remove particulate material from a system; an industrial application would be the controlling of pollutants. Particles or droplets are removed from industrial residues, for instance water or gas. Solid pollutants can also be separated from the gas by devices like a cyclone separator or an electrostatic precipitator. In the case of a filter, it is obviously in the manufacturer's interest that the deposition is *maximized*.

However, the background for the work behind this thesis is the following incentive to *minimize* the deposition: In a bioenergy power plant, some biomass is combusted. This results in gases carrying thermal energy to the heat exchangers, pipes carrying the working fluid, to which the thermal energy is transfered. These pipes are in essence cylinders, typically with circular cross sections. In the further process, the thermal energy now carried by the working fluid runs the turbines generating electricity. At the stage of com-

bustion, residuals like ash particles are created. These are carried along with the gas flow, and some are deposited on the heat exchangers, as the pipes cross the gas flow, as indicated in figure 1.1. A result of this is that an insulating layer is formed on the pipes, and hence there will be a reduction in the energy conversion efficiency defined as

$$\eta_{\text{eff}} \equiv \frac{E_{\text{out}}}{E_{\text{in}}}, \tag{1.1}$$

where E_{out} is the energy output and E_{in} the energy put into the system. Clearly, η_{eff} is wanted to be as high as possible, making it desirable to minimize the deposition.

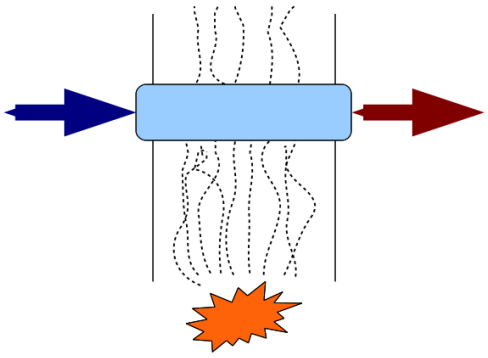

Figure 1.1: Simplified schematic overview of a biomass fueled combustion plant. The particle containing fluid flows upwards and transfers heat to the heat exchanger, where the temperature of the heat carrying fluid is raised.

Originally, design of these systems was primarily based on empirical foundation (Crowe et al., 1998 [2]). With numerical analysis and simulation, progress has been made towards improved quantification of such systems. The fact that the combustion also emits pollutants that one might want to remove, is not of relevance in this study. The gas-particle flow considered in the present work is a dispersed phase flow, where the particles constitute the dispersed phase and the fluid is the continuous phase. It is known that in a combustion facility like the one described above, turbulence occurs in the flow. Although the intensity of the turbulence occuring in the real-world applications is unknown, it is of interest to numerically investigate the turbulence's impact on the particle deposition. This is because turbulence has an influence on the behaviour of the particles and affects the deposition and consequently η_{eff}. In addition, turbulence is a phenomenon still in need of further investigation. A reason for doing this numerically is the possibility to attain idealized situations with high flexibility in the controlling of input and output variables.

1.2 Basic concepts

A brief introduction to some concepts important in the present work is given in this section. The theory presented in chapter 2 will go more in depth.

1.2.1 The Reynolds number

The Navier-Stokes equation is introduced in the next chapter. The ratio between the magnitudes of the convective and the dissipative terms in this equation, i.e. the spatial acceleration of the fluid element and the divergence of stress respectively, is the Reynolds number

$$\mathrm{Re} = \frac{U^2/L}{\nu U/L^2} = \frac{UL}{\nu}. \tag{1.2}$$

Here, U is a characteristic velocity in the flow scenario, L a characteristic length and ν the kinematic viscosity of the fluid. The Reynolds number is advantageous when analyzing the nature of a specific flow, as all flows with the same Reynolds number have the same physical properties. Also, a fluid flow scenario may be characterized by more than one Reynolds number. A particle-laden flow like the one treated in this work has for instance one Reynolds number related to the characteristics of the particles as well as one expressed by the geometry of the cylinder and the properties of the fluid.

1.2.2 Turbulence

In fluid dynamics, two basic fluid regimes exist: the laminar and the turbulent. While the values of the fluid properties, such as the velocity and the pressure, in the laminar regime are in principle easy to calculate, this is not the case for fluid flows in the turbulent regime. Exact analytical solutions do not exist, even for the most elementary turbulent flows. On the contrary to the predictable nature of the laminar flow, the turbulent flow is a random process. The values of the flow variables cannot in advance be uniquely determined at one specific point at one specific time instant. However, its statistical properties can be considered to give a description of the flow, even if the behaviour in detail is unpredictable. The statistical analysis of a turbulent flow starts with expressing a fluid property as

$$\boldsymbol{A} = \bar{\boldsymbol{A}} + \boldsymbol{A'}, \tag{1.3}$$

where the property $\boldsymbol{A}$ can be the velocity field $\boldsymbol{u}$, or a scalar like the pressure. The mean value of the velocity is then $\bar{\boldsymbol{u}}$, and $\boldsymbol{u'}$ denotes its fluctuations

around the mean. Turbulence is a three-dimensional phenomenon, implying the velocity has fluctuations in every direction: u', v' and w' in the spatial directions x, y and z respectively.

In a flow domain with volume V, the root mean square of the velocity fluctuations,

$$u_{\text{rms}} = \sqrt{\frac{1}{V}\int \boldsymbol{u'}^2 \mathrm{d}V}, \tag{1.4}$$

is valuable for analyzing the magnitude of the velocity fluctuations, and gives indications on how intense the overall turbulence is.

As $\boldsymbol{A}$ expresses random values attained throughout the course of the flow, it is a difficult, and still an unsolved, problem to find a deterministic model for the turbulent flow. So numerical tools are essential when broadening an understanding of these flows. And as most realistic flows in the industry and everyday life have a turbulent nature, a wide understanding is indeed crucial.

A turbulent flow is characterized by a wide range of different time and space scales. The length scales can be expressed in terms of the diameter of the different turbulent eddies, whereas the eddy turnover time represents the time scales. To get a fully valid solution for the flow evolving, all these scales should be resolved, like it is done in a Direct Numerical Simulation (DNS). A brief description of DNS is given in section 3.1 in chapter 4.

1.2.2.1 Kolmogorov scales

The smallest turbulence scales are called the *Kolmogorov scales*. At this level, the viscosity becomes important in the energy dissipation cascade. As the turbulent state is established, continued turbulence is generated in the form of unstable eddies. The large-scale eddies initiated by the turbulence create smaller eddies, which again generate smaller ones in a continuous series or cascade. Throughout this cascade, energy is passed on until it is dissipated by the viscosity at the Kolomogov scale. At this scale, the energy associated with the smallest eddies is dissipated and converted into thermal internal energy. This explains why turbulence is a high-Reynolds number phenomenon: With a low Reynolds number, the viscous term gets too dominating for the cascade to go on and the energy is dissipated at the largest scales. The effective mixing and mean flux of energy from large to small scales in turbulent flows makes turbulence attractive for instance in combustion. Whether a flow is turbulent or laminar, will depend on its geometric properties and the nature of the specific flow. Hence it cannot be said in a simple manner that a specific magnitude of the Reynolds number corresponds to the one or the other fluid regime. A flow can exhibit instabilities and still have a predictable behaviour and thus be in the laminar regime.

1.2.3 Vorticity

In the present work, the vorticity

$$\boldsymbol{\omega} = \nabla \times \boldsymbol{u} \tag{1.5}$$

of the flow is studied. Stokes' theorem from vector calculus gives

$$\int\int_{\mathcal{S}} (\nabla \times \boldsymbol{u}) \cdot \boldsymbol{n} \mathrm{d}S = \oint_{\mathcal{C}} \boldsymbol{u} \cdot \mathrm{d}\boldsymbol{l} = \int\int_{\mathcal{S}} \boldsymbol{\omega} \cdot \boldsymbol{n} \mathrm{d}S. \tag{1.6}$$

From this, a physical interpretation of $\boldsymbol{\omega}$ can be established. By letting the surface $\mathcal{S}$ be plane with unit normal vector $\boldsymbol{n}$, bounded by a small circle $\mathcal{C}$ with the unit radius vector $\boldsymbol{r}$, the unit vector $\boldsymbol{l} = \boldsymbol{n} \times \boldsymbol{r}$ is tangential to $\mathcal{C}$. Now, the angular velocity of points at $\mathcal{C}$ equals $\boldsymbol{r} \times \boldsymbol{u}$. The projection of this angular velocity in the normal direction, averaged over the surface area, becomes

$$\begin{aligned} \frac{1}{2\mathcal{S}} \oint_{\mathcal{C}} \boldsymbol{n} \cdot (\boldsymbol{r} \times \boldsymbol{u}) \mathrm{d}l = \frac{1}{2\mathcal{S}} \oint_{\mathcal{C}} \boldsymbol{u} \cdot (\boldsymbol{n} \times \boldsymbol{r}) \mathrm{d}l = \frac{1}{2\mathcal{S}} \oint_{\mathcal{C}} \boldsymbol{u} \cdot \boldsymbol{l} \mathrm{d}l \\ = \frac{1}{2\mathcal{S}} \int\int_{\mathcal{S}} \boldsymbol{\omega} \cdot \boldsymbol{n} \mathrm{d}S \approx \frac{1}{2} \boldsymbol{\omega} \cdot \boldsymbol{n}. \end{aligned} \tag{1.7}$$

Here, a standard vector identity has been used at the first equal sign, (1.6) at the last equal sign and the approximation is due to the small surface area $\mathcal{S}$. As (1.7) holds for any $\boldsymbol{n}$, it is concluded that $\boldsymbol{\omega}$ is twice the angular velocity of the fluid.

Areas in a flow with concentrated vorticity are called *vortices*. A flow with a non-zero vorticity contains rotation, and turbulent flows have small-scale random vorticity. Rotational flows can also be laminar, but the intense small-scale random vorticity fluctuations are characteristic for the turbulent regime. These randomly directed fluctuations have a magnitude much larger than the mean vorticity. As $\boldsymbol{\omega}$ contains the spatial derivatives of $\boldsymbol{u}$, it expresses the fine-scale behaviour of the $\boldsymbol{u}$-field. This implies that the spatial scale for the fluctuations in $\boldsymbol{\omega}$ is among the smallest of all turbulence scales.

1.2.4 Particles in a flow around a cylinder

The two-dimensional flow around the cross section of a cylinder is simulated in the present work. Based on the mean flow velocity U_0, the cylinder diameter D and the kinematic viscosity ν of the fluid, the two Reynolds numbers used are $\mathrm{Re_c} = 421$ and $\mathrm{Re_c} = 1685$. The numerical values can be found in appendix B.

A *Von Kármán vortex street* is seen in the wake of a cylinder in a cross flow when $\mathrm{Re_c}$ exceedes a certain number, typically around 50 (Pozrikidis, 2001 [3]). The vortices arise as eddies shed from each side of the cylinder, in an alternating manner, leading to two rows of counter-rotating vortices. At a certain distance downstream, the vortices turn gradually turbulent from $\mathrm{Re_c} \sim 200$ onwards (Haugen & Kragset, 2010 [4]). On the contrary, the boundary layer of the cylinder becomes turbulent at $\mathrm{Re_c} \sim 2 \cdot 10^5$. This is in agreement with the fact that at increasing Reynolds number, viscous forces are significant inside the boundary layer, but can be neglected outside their edges (Pozrikidis, 2001 [3]).

An effect of putting particles into a turbulent flow is that the particles inherit the behaviour of the flow field. The extent to which this is the case obviously depends on the inertial characteristics of the particles in question, which will be discussed in later chapters. Particles that are influenced by the turbulent motions attain complex unsteady motions which may result in nonuniform spatial distribution of particles and hence particle segregation (Brennen, 2005 [5]). On the other hand, a modification of the turbulence itself can be experienced; the turbulence may be damped due to the presence of the particles, or enhanced by the particle wakes produced by the motion of the particles relative to the fluid. As the present work considers only one-way-coupling, i.e. the effect of the turbulence on the particles and not vice versa, the possible modification of turbulence by the presence of particles will not come into play.

An effect of relevance in the present work is the accumulation of particles in shear zones in between vortices; this is due to the fact that particles are centrifuged out by the turbulent eddies. A more theoretical treament of this will be given in the next chapter. Experimental observations and numerical calculations indicate that these local particle accumulations again intensify the velocity fluctuations of the flow (Xu & Subramaniam, 2010 [6]), but due to one-way coupling, this is again out of the scope of the present work.

1.3 Aim and overview of thesis

There has been found few previous studies directly comparable to what is described in this thesis. Guha (2008) [7] provides a fine review on existing findings, theory and methods in research on deposition of particles in both turbulent and laminar flows. Some experimental studies have been conducted in the past. A higher Reynolds number study was for example done by Douglas & Ilias (1988) [8]. Several recent studies on particle dispersion in turbulent flow have often been by means of numerical methods, where for

example Marchioli et al. (2003) [9] and Luo et al (2006) [10] applied DNS, but focused on pipe flow and material erosion respectively. The DNS approach in the present work was also implemented for the studying of particle deposition on a cylinder by Haugen & Kragset (2010) [4] and Bjørnstad (2010) [11]. Haugen & Kragset (2010) [4] ran simulations of laminar flow also at $\mathrm{Re_c} = 421$ and $\mathrm{Re_c} = 1685$, while the effect of turbulence on the deposition of particles in a flow at $\mathrm{Re_c} = 421$ was studied by Bjørnstad (2010) [11]. Being the only similar studies found, these are the main foundation when discussing the results of the present work.

The goal of the present work is to investigate particles dispersed in a fluid flow and numerically study their behaviour, with specific weight on the deposition of particles on a cylinder in the flow domain. The effect of the presence of turbulence on the particles and their deposition is studied and discussed, as well as how the two differing values of the Reynolds number influence the results.

The contents of this thesis consists of the following. In chapter 2, the physical theoretical foundation is laid. This consists of relevant equations from fluid and particle dynamics, introduction of quantities necessary for the analysis of the results and some turbulence theory relevant for particle-laden flows. Chapter 3 gives a short introduction to Computational Fluid Dynamics (CFD) as a tool to solve fluid flow problems, and more specifically explains the principles of Direct Numerical Simulation (DNS) as a CFD technique. This is followed by a presentation of the numerical method used in the present work. This includes primarily a description of the DNS code used, simulation procedures and the boundary conditions for fluid and particles. Results are presented and discussed in chapter 5, while a more comprehensive discussion on the particle deposition under turbulent conditions is given in chapter 6. The findings of the work are thereafter summarized in the conclusion, finishing the main part of the thesis.

Chapter 2

Theory

The basic equations describing the motion of the fluid and the particles are presented in the following. In addition, some turbulence theory and theory on particle clustering in turbulence is contained.

2.1 Equations from fluid dynamics

The equations for the fluid motion are solved in an Eulerian manner, meaning that they are solved at fixed points at successive time steps, i.e. with the observer being at rest. The principal aim is to find solutions for the velocity, pressure and density of the flow at all grid points. The first equation is a result of the fact that the total rate of mass change within a physical system is zero, namely the continuity equation

$$\frac{\partial \rho}{\partial t} + \nabla \cdot (\rho \boldsymbol{u}) = 0, \tag{2.1}$$

where ρ is the density and $\boldsymbol{u}$ the velocity of the fluid. Furthermore, by applying the principle that the momentum change in a system equals the sum of external forces, the Navier-Stokes equation is given as

$$\rho \frac{D\boldsymbol{u}}{Dt} = \boldsymbol{f} - \nabla p + \nabla \cdot \mathbb{T}. \tag{2.2}$$

This resembles Newton's second law. The substantive or material derivative

$$\frac{D\boldsymbol{u}}{Dt} = \frac{\partial \boldsymbol{u}}{\partial t} + \boldsymbol{u} \cdot \nabla \boldsymbol{u} \tag{2.3}$$

expresses the acceleration, consisting of two terms since the derivative is taken along a moving path. Its first term denotes the local change in velocity

with time, while the nonlinear term expresses the change due to convection. On the right hand side of (2.2), the volume force density $\boldsymbol{f}$, the pressure p and the 3×3 stress tensor for a Newtonian fluid

$$\mathbb{T} = \rho\nu\Big[(\nabla \boldsymbol{u}) + (\nabla \boldsymbol{u})^T\Big] - \frac{2}{3}\rho\nu\nabla \cdot \boldsymbol{u}\mathbb{I} \tag{2.4}$$

are contained in terms expressing the volume forces, the pressure gradient and the divergence of shear stress. In (2.4), $\mathbb{I}$ is the identity matrix. The volume force density $\boldsymbol{f}$ can in the general case be e.g. gravity per unit volume. Furthermore, the divergence of shear stress, $\nabla \cdot \mathbb{T}$, is a dissipative term that converts kinetic energy into heat.

As $\boldsymbol{u}$ is three-dimensional, one additional equation is needed to get a closed system. To be able to solve for all five unknowns $\boldsymbol{u}$, p and ρ, the ideal gas equation of state,

$$p = c_s^2\rho, \tag{2.5}$$

is valid as the flow is compressible and isothermal, and hence all variables can be resolved. Here, $c_\mathrm{s} = \sqrt{\partial p/\partial \rho}$ is the speed of sound.

2.2 The motion of the particles

A particle follows a trajectory in the fluid, at any time indicated by the instantaneous centre of mass position $\boldsymbol{x}$ of the particle. The particle is tracked from a single time step to the next, different from the fluid properties, which are resolved by the equations in section 2.1 at the fixed grid points. The particle motion is described by

$$\frac{d}{dt}(m_\mathrm{p}\boldsymbol{v}) = \boldsymbol{F}, \tag{2.6}$$

and the particle velocity

$$\frac{d\boldsymbol{x}}{dt} = \boldsymbol{v}. \tag{2.7}$$

This is the general Lagrangian form of the equations; particles are tracked throughout the evolving of time. The particle mass m_p is constant and hence $d\boldsymbol{v}/dt$ is explicitly given by (2.6). The sum of all forces acting on the particle is represented by $\boldsymbol{F}$. Some forces acting on a particle in a flow scenario are mentioned by Talbot et al. (1980) [12]. Among these forces are the drag force, interaction forces between the particle and surrounding particles and between the particle and walls in the system, Brownian diffusion, electromagnetic forces, the thermophoretic force and gravity. In this work, gravity

is negligible, as all particles are too small for it to have any significant effect. As there in the present work are periodic boundary conditions at the walls, explained in chapter 4, particle-wall interactions are non-existing. In a more complex description of the problem, it would be fruitful also to include the thermophoretic force, which arises due to different particles responding differently to temperature gradients. These further issues are taken into account e.g. by Guha (2008) [7], who describes how the various forces can be implemented in a more general description of the particle-laden flow. But for the implementation of the equations here, the single particle behaviour is focused on and thus, the drag force $\boldsymbol{F}_{\mathrm{D}}$ is the only force considered. This is legitimate, due to low particle concentration in typical industrial boilers (Haugen & Kragset 2010 [4]). Hence, $\boldsymbol{F}$ in (2.6) is set equal to $\boldsymbol{F}_{\mathrm{D}}$. This force arises due to the particle's motion relative to the fluid. The drag force is, as given in Crowe et al. (1998) [2],

$$\boldsymbol{F}_{\mathrm{D}} = \frac{1}{2}\rho C_{\mathrm{D}} A|\boldsymbol{u} - \boldsymbol{v}|(\boldsymbol{u} - \boldsymbol{v}), \tag{2.8}$$

where C_{D} is the drag coefficient. The particle, being spherical with a radius r_{p}, has a cross-sectional area $A = \pi r_{\mathrm{p}}^2$.

As the velocity of the particles does not affect the behaviour of the fluid flow field, one-way coupling between fluid and particles is applied. One-way coupling is typically applied in studies like this, when the main interest is the dispersion of particles in turbulence (Squires & Eaton, 1990 [13]). Also, any forces from the injected particles acting on the fluid flow can be neglected, due to the particles' small size, hence one-way coupling is appropriate. These forces would otherwise be implemented as terms in $\boldsymbol{f}$ in (2.2).

For situations where particles are very small, the fluid has to be looked upon as separate particles, rather than a continuum. If so, $|\boldsymbol{F}_{\mathbf{D}}|$ is reduced by division by the empirically found Stokes-Cunningham factor

$$C_{\mathrm{C}} = 1 + \frac{\lambda}{r_{\mathrm{p}}}(1.257 + 0.4e^{-1.1r_{\mathrm{p}}/\lambda}), \tag{2.9}$$

where λ is the mean free path for a particle in the fluid. As is seen from (2.9), C_{C} is close to 1 in case of $\lambda/r_{\mathrm{p}} \ll 1$, leading to a very low reduction in the drag force. So when using (2.8) for the drag force, the results in this thesis are valid for a flow primarily regarded as a continuum. It is stated by Crowe et al. (1998) [2] that $\lambda/2r_{\mathrm{p}} \lesssim 10^{-3}$ corresponds to continuum flow, which is the case for most particles sizes explored in this thesis. The drag coefficient C_{D} depends on the particle characteristica, which can be expressed by the particle Reynolds number, or the dispersed phase relative Reynolds number,

$$\mathrm{Re}_{\mathrm{p}} = \frac{d_{\mathrm{p}}|\boldsymbol{u} - \boldsymbol{v}|}{\nu}, \tag{2.10}$$

where $d_\mathrm{p} = 2r_\mathrm{p}$ is the characteristic size of the particle. The drag coefficient used in equation (2.8) is given by (Haugen & Kragset, 2010 [4])

$$C_\mathrm{D} = \begin{cases} 0.44 & \text{if } \mathrm{Re_p} > 1000, \\ \frac{24}{\mathrm{Re_p}}(1 + 0.15\mathrm{Re_p}^{0.687}) & \text{if } \mathrm{Re_p} \lesssim 1000. \end{cases} \tag{2.11}$$

The particle Reynolds number $\mathrm{Re_p}$, given by (2.10), will typically be a low number*, meaning that the lower case in (2.11) is used. By using (2.10), the spherical particle mass density $\rho_\mathrm{p} = 6m_\mathrm{p}/\pi d_\mathrm{p}^3$ and defining $f_\mathrm{D} \equiv 0.15\mathrm{Re_p}^{0.687}$, (2.8) can be written in a form resembling Newton's second law, namely

$$\boldsymbol{F_\mathrm{D}} = \frac{m_\mathrm{p}}{\tau_\mathrm{p}}(\boldsymbol{u} - \boldsymbol{v}), \tag{2.12}$$

where the particle response time

$$\tau_\mathrm{p} = \frac{m_\mathrm{p} C_\mathrm{C}}{3\pi\nu\rho d_\mathrm{p}} = \frac{\rho_\mathrm{p}}{\rho}\frac{d_\mathrm{p}^2 C_\mathrm{C}}{18\nu(1 + f_\mathrm{D})} \tag{2.13}$$

expresses the time it takes for a particle to respond to changes in the flow velocity. Here, $\boldsymbol{F_\mathrm{D}}$ has been divided by C_C and this factor is kept also in the simulations for general applicability.

The particle response time is helpful when establishing dimensionless parameters characterizing the flow. This can be exemplified, like in Crowe et al. (1998) [2], by noticing how (2.12) implies that the expression for the particle acceleration is

$$\frac{d\boldsymbol{v}}{dt} = \frac{(\boldsymbol{u} - \boldsymbol{v})}{\tau_\mathrm{p}}. \tag{2.14}$$

Solving this differential equation in scalar form with u held constant and an initial particle velocity of zero, gives $v = u(1 - \exp(-t/\tau_\mathrm{p}))$. This clarifies the role of τ_p as a dimensionless parameter describing how fast a particle at rest achieves a certain velocity when influenced by the fluid flow, cf. figure 2.1.

Furthermore, it is appropriate to introduce the Stokes number

$$\mathrm{St} = \frac{\tau_\mathrm{p}}{\tau_\mathrm{f}}, \tag{2.15}$$

where τ_f analogously to the particle response time must be a characteristic time for the fluid. St indicates to which extent the particle inertia's influence its motion, compared to the influence from the fluid flow. The following applies for the Stokes number:

*In the simulations, particles of diameter d_p in the order range $10^{-6} - 10^{-4}$ m are used, and the kinematic viscosity is in the order of 10^{-4}.

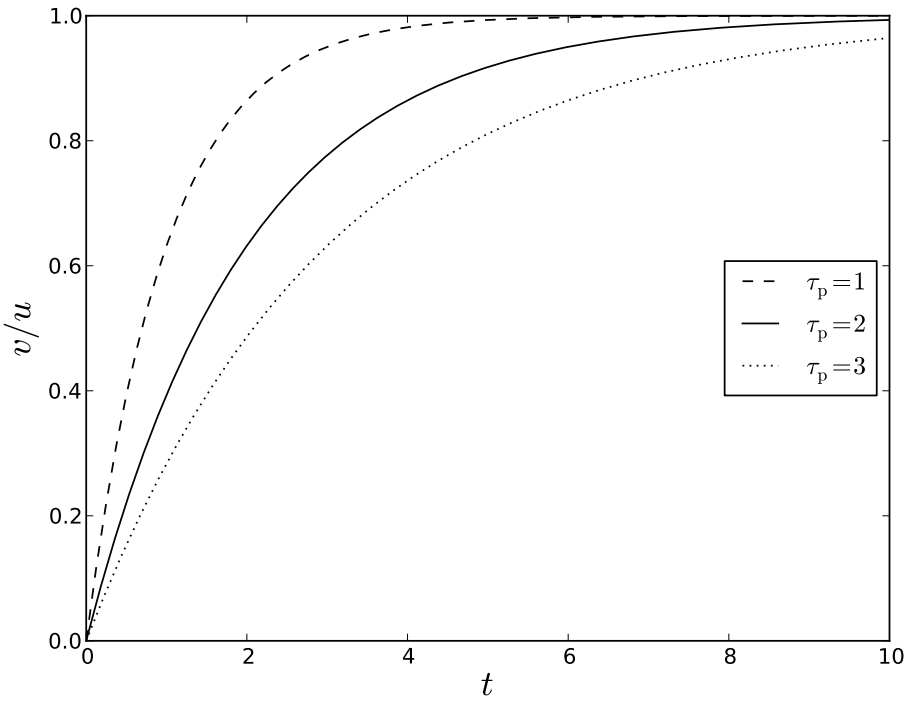

Figure 2.1: The value of the particle response time τ_p is seen to influence how fast the particle velocity v reaches the value of the fluid velocity u.

$$\begin{cases} \mathrm{St} \gg 1 \Leftrightarrow \text{particle moves in straight lines independent of the flow,} \\ \mathrm{St} \ll 1 \Leftrightarrow \text{particle follows the flow streamlines strictly.} \end{cases}$$

A characteristic time for the flow in this work is described by the cylinder dimensions and hence

$$\tau_\mathrm{f} = \frac{r_\mathrm{c}}{U_0}, \tag{2.16}$$

where r_c is the radius of the cylinder and U_0 the mean velocity of the flow. To investigate the motion of the particle as a function of St, equations (2.14), (2.15) and (2.16) are combined. This yields

$$\frac{d\boldsymbol{v}}{dt} = \frac{U_0}{r_\mathrm{c}\mathrm{St}}(\boldsymbol{u} - \boldsymbol{v}). \tag{2.17}$$

Hereby it is seen that the Stokes number is related to the particle's inertia; a larger St gives a decreasing particle acceleration.

2.3 Turbulent kinetic energy

The two-point correlation tensor or Reynolds stress tensor

$$R_{ij}(\boldsymbol{r},t) = \overline{u_i(\boldsymbol{x},t)u_j(\boldsymbol{x}+\boldsymbol{r},t)} \tag{2.18}$$

can provide information on the size of turbulent eddies. The tensor R_{ij} is the mean of all correlations, or covariances, between the velocity components of the flow field. In the case of homogeneous turbulence, R_{ij} is independent of $\boldsymbol{x}$, because the statistical properties remain the same under any arbitrary spatial displacement, i.e. under a translation of the reference system. The three-dimensional Fourier transforms of R_{ij} can be defined as the spectral functions

$$\Phi_{ij}(\boldsymbol{k},t) = \frac{1}{(2\pi)^3}\int R_{ij}(\boldsymbol{r},t)e^{-i\boldsymbol{k}\cdot\boldsymbol{r}}\mathrm{d}\boldsymbol{r}, \tag{2.19}$$

where $\mathrm{d}\boldsymbol{r}$ denotes a volume integral. The motivation behind the Fourier transform is that the velocity field itself can be expressed as a Fourier series in terms of

$$\boldsymbol{u}(\boldsymbol{r},t) = \sum_{\boldsymbol{k}} \tilde{u}(\boldsymbol{k},t)e^{i\boldsymbol{k}\cdot\boldsymbol{r}}, \tag{2.20}$$

where $\tilde{u}(\boldsymbol{k},t)$ are the Fourier components. Furthermore, the inverse transform of (2.19) is

$$R_{ij}(\boldsymbol{r},t) = \int \Phi(\boldsymbol{k},t)e^{i\boldsymbol{k}\cdot\boldsymbol{r}}\mathrm{d}\boldsymbol{k}, \tag{2.21}$$

an integral over the entire wavenumber $\boldsymbol{k}$ space. If now $\boldsymbol{r} = 0$, t is omitted for convenience and j is set equal to i, it is found that

$$\frac{1}{2}R_{ii} = \frac{1}{2}\langle u_i u_i\rangle = \frac{1}{2}\int \Phi_{ii}(\boldsymbol{k})\mathrm{d}\boldsymbol{k}. \tag{2.22}$$

The turbulent kinetic energy is hereby expressed as an integral over $\boldsymbol{k}$, and equation (2.19) can be seen as an energy distribution in wavenumber space. This means if the correlation tensor R_{ij} is calculated by a numerical simulation, the three dimensional energy spectrum is found by

$$E(\boldsymbol{k}) = \frac{1}{2}\sum_{i=1}^{3}\tilde{u_i}(\boldsymbol{k})\tilde{u_i}^*(\boldsymbol{k}). \tag{2.23}$$

Here, the asterisk denotes the complex conjugate.

2.4 Kolmogorov theory and the energy spectrum

In the following, some aspects of the turbulence theory of Kolmogorov are discussed. Some introducing concepts were discussed in section 1.2.2. The theory of Kolmogorov (recapitulated for instance by Pope (2000) [14]) describes the transfer and dissipation of energy throughout the cascade of eddies of decreasing size; how much energy is contained in eddies of different size and where the energy is dissipated. Here, the *eddy* is a turbulent rotational motion that spans a region of size L_{eddy}. Across this region, the eddy is relatively coherent, i.e. its shape does not change. Associated to the eddy size L_{eddy}, is a characteristic velocity u_{eddy}. The largest eddies are of the size l_0; these are the energy-containing eddies, and l_0 is called the *integral scale* of turbulence. The characteristic velocity at this scale is in the order of u_{rms}. Thus, these eddies have kinetic energy in the order of u_{rms}^2. So with an eddy turnover time τ_0 at the integral scale, the rate of energy transfered at this scale is

$$T_0 \sim \frac{u_{\text{rms}}^2}{\tau_0} \sim \frac{u_{\text{rms}}^3}{l_0}. \tag{2.24}$$

As already stated, dissipation takes place at the end of the energy cascade. The rate ϵ of dissipation of energy is proportional to T_0, as the turbulent energy contained at the integral scale is carried along the cascade. The Kolmogorov microscales can be deduced as given in Pope (2000) [14], where the Kolmogorov length scale is found to be

$$\eta = (\frac{\nu^3}{\epsilon})^{1/4}, \tag{2.25}$$

and the time scale

$$\tau_\eta = (\frac{\nu}{\epsilon})^{1/2}. \tag{2.26}$$

Here, ϵ is the average energy dissipation rate per mass. From this, the Kolmogorov velocity will be given as

$$u_\eta = \frac{\eta}{\tau_\eta} = (\epsilon\nu)^{1/4}. \tag{2.27}$$

These scales characterize the smallest, dissipative turbulent eddies, a fact that is verified by noting that the Reynolds number based on these scales is $\text{Re}_\eta = \eta u_\eta/\nu = 1$. This indicates effective dissipation and viscous dominance at this scale. It is seen that

$$\epsilon = \frac{u_\eta^2}{\tau_\eta} \sim \frac{u_\eta^3}{\eta}, \tag{2.28}$$

which is sensible when looking at (2.24).

The energy spectrum $E(k)$ decays proportionally to $k^{-5/3}$ for a certain k range, the *inertial subrange*, where energy is transfered to succesively smaller eddies. In the logarithmic plot, cf. figure 3.1, this is seen by a linear slope of -5/3 in the medium high k range. This shape can be determined from dimensional analysis, using the fact that the shape of $E(k)$ is dependent only on ϵ and k. For higher wavenumber the decay is steeper. The universal forms of the spectra at medium wavenumbers, in the *universal equilibrium range*, are found to be in accordance to Kolmogorov's hypothesis of local isotropy (Pope, 2000 [14]). This states that the small-scale eddies, where $L_{\text{eddy}} \ll l_0$, are statistically isotropic, meaning their behaviour is the same in all directions: $\bar{u'^2} = \bar{v'^2} = \bar{w'^2}$. According to Kolmogorov, this loss of directional information happens because of the chaotic reduction of eddy scales down along the energy cascade. In addition, geometrical information also is lost throughout the energy cascade, giving all small scale eddies the same shape.

The inertial subrange is found within the high wavenumber range, while the *dissipation range* corresponds to the highest k. For the lowest k, i.e. to the left of the inertial subrange, the *energy-containing range* is found. The magnitude of the length scales l is in the inertial subrange such that $\eta \ll l \ll l_0$, where l_0 is the scale at which the largest eddies appear. In the energy-containing range, $E(k)$ does not have any universal form, but is rather dependent on the particular flow (Pope, 2000 [14]). The theory of Kolmogorov holds perfectly for very high Reynolds numbers; the shape of the spectrum can deviate in case of the Reynolds numbers considered in the present work.

2.5 Particle clustering in turbulence

A well-documented effect (see e.g. Chun et al. (2003) [15] or Squires & Eaton (1991) [16]) of the presence of turbulence in a particle-laden flow is the local clustering of particles, i.e. particle concentrations higher than the mean value in certain regions in the flow field, while the concentration is lower than the mean value in other regions. Particle clustering may influence different aerosol processes such as settling, evaporation, interparticle collisions and also formation of convective clouds in the atmosphere (Salazar et al., 2008 [17]). Particles get thrown out of high vorticity regions, namely the turbulent eddies, and are accumulated in the straining-flow regions between the eddies. The phenomenon is also called *preferential concentration*, thoroughly explained for example in the studies by Aliseda et al. (2002) [18] and

Wood et al. (2005) [19]. Particle clustering or preferential concentration of particles implies a spatially inhomogeneous particle concentration. For the preferential concentration to take place, the eddy must transfer an inertia to the particle. Thus, the particle response time τ_p must be in order of the eddy's characteristic time τ_eddy. Being the time it takes for the eddy to make one turnover, it can be expressed by

$$\tau_\mathrm{eddy} = \frac{L_\mathrm{eddy}}{u_\mathrm{rms}}, \tag{2.29}$$

where L_eddy is the typical size of a turbulent eddy. According to Aliseda et al. (2002) [18], there has been some controversy regarding which fluid time scale is most appropriate to use, as the eddies decrease in size down along the energy cascade. For example Aliseda et al. (2002) [18] and Wang & Maxey (1993) [20] use the Kolmogorov time scale τ_η. The highest vorticity gradients occur at the Kolmogorov scale, thus this is a natural choice as the preferential concentration is most significant in high vorticity areas. Previous work has shown that with $\tau_\mathrm{eddy} = \tau_\eta$ as time scale, the preferential concentration is at its maximum for $\mathrm{St}_\mathrm{eddy} = \tau_\mathrm{p}/\tau_\mathrm{eddy} \sim 1$ (Salazar et al., 2008 [17]). This is explained as follows: If $\tau_\mathrm{eddy} \gg \tau_\mathrm{p}$, then the rotation of the eddy is too slow and the particle follows the eddy perfectly. So a very light particle behaves more as a fluid element. On the contrary, when $\tau_\mathrm{eddy} \ll \tau_\mathrm{p}$, the particle will not have time to respond to the fast motion of the eddy. In the cases where $\mathrm{St}_\mathrm{eddy} \sim 1$, the particle responds to the eddy motion and is thrown out of the high vorticity region of the eddies; the particles are 'centrifuged' outwards. This extra inertia of the particles may also lead to higher deposition at a cylinder in the flow domain, as the acceleration gained from the turbulent eddies is present in addition to the convection related to the fluid motion. This effect comes into play only for particles gaining this inertia close to the cylinder. It is also found that the settling velocity of particles increases monotonically with the local particle concentration (Aliseda et al., 2002 [18]).

As the particle number density is largely dependent on the value of the vorticity, a correlation between these two is needed to establish a quantification of the effect of preferential concentration. A way to do this (Squires & Eaton, 1990 [13]) is to use the strain rate and rotation rate tensors, defined as

$$S_{ij} = \frac{1}{2}\left(\frac{\partial u_i}{\partial x_j} + \frac{\partial u_j}{\partial x_i}\right) \tag{2.30}$$

and

$$\Omega_{ij} = \frac{1}{2}\left(\frac{\partial u_i}{\partial x_j} - \frac{\partial u_j}{\partial x_i}\right) \tag{2.31}$$

respectively[†]. By using these, we can express the second invariant of the deformation tensor, defined to be

$$-2II_{\mathrm{d}} \equiv \frac{\partial u_i}{\partial x_j}\frac{\partial u_i}{\partial x_j}, \tag{2.32}$$

as

$$\begin{aligned} -2II_{\mathrm{d}} &= (S_{ij} + \Omega_{ij})(S_{ji} + \Omega_{ji}) \\ &= S_{ij}S_{ji} + \Omega_{ij}\Omega_{ji} + S_{ij}\Omega_{ji} + S_{ji}\Omega_{ij} \\ &= S_{ij}S_{ji} - \Omega_{ij}\Omega_{ji}, \end{aligned} \tag{2.33}$$

where the antisymmetry of the rate of rotation tensor and the symmetry of the rate of strain tensor, i.e. $\Omega_{ij} = -\Omega_{ji}$ and $S_{ij} = S_{ji}$, is used to achieve the last line. From (2.33) it is concluded that the second invariant of the deformation tensor can be written as

$$II_{\mathrm{d}} = -\frac{1}{2}(S^2 - \frac{1}{4}\omega_j\omega_j), \tag{2.34}$$

where S is the magnitude of the rate of strain tensor and ω_j is the j-component of the vorticity of the flow field. As also stated by Squires & Eaton (1991) [16], the properties of II_{d} can be summed up as

$$II_{\mathrm{d}} \begin{cases} > |II_{\mathrm{e}}| & \Leftrightarrow \text{high } \omega \text{ and low } n, \\ < -|II_{\mathrm{c}}| & \Leftrightarrow \text{low } \omega \text{ and high } n, \end{cases} \tag{2.35}$$

where $|II_{\mathrm{e}}|$ and $-|II_{\mathrm{c}}|$ denote positive and negative threshold values respectively. From this, a flow field classification can be made, explained by Squires & Eaton (1991) [16]. Here, the turbulent flow field is divided into four zones, namely eddy, convergence, streaming and rotational zones. The strongly swirling motions are found in the vorticity containing eddy zones. This corresponds to the upper case in (2.35), where the irrotational strain is small compared to the vorticity, leading to curved streamlines. In the interior of the zone, the pressure p_{in} is lower than a certain threshold value p_{e}, due to the rotational nature of the fluid in this domain. The convergence zone has on the contrary highly straining motion and strong convergence and divergence of streamlines, corresponding to the lower case in (2.35), where II_{d} is less than $-|II_{\mathrm{c}}|$, the threshold value defining the convergence region. Here the pressure stays above the pressure threshold value p_{c} defining the region. It follows that convergence zones are regions where stagnation in the flow is

[†]The Einstein summation convention is used here. The velocity gradient tensor $\partial u_i/\partial u_j$ is expressed by $\nabla \boldsymbol{u}$ in vector form.

found. Furthermore, the streaming zone is defined by $|II_\mathrm{d}| < \min(II_\mathrm{e}, II_\mathrm{c})$ and the rotational zone by the same criterion for the value of the second deformation tensor as the eddy zone, but by the pressure criterion $-p_\mathrm{e} < p_\mathrm{in} < p_\mathrm{c}$. Thus, the rotational zone also possesses primarily vorticity, but is not characterized by curved streamlines like the eddy zones. In the streaming zones, the speed is high while the velocity vectors have low curvature.

Chapter 3

Computational Fluid Dynamics

As turbulent flows cannot be solved analytically, numerical methods are needed. A numerical scheme in general has a spatial discretization that constitutes an approximation of the derivatives of a finite number of variables. The spatial representation is prescripted to march forward in time, by means of discretized time steps, from some initial conditions. Finite difference methods represent values at a discrete grid of points and approximate the spatial derivatives by differencing. With a grid point distance Δx and time steps Δt, for a proper numerical method, when $\Delta x \to 0$ and $\Delta t \to 0$, the numerical solution must converge towards the 'true' solution. Whether this solution reflects the real-world situation simulated, depends on e.g. models used, restrictions made and the numerical scheme itself. The difference between the numerical solution and the exact solution is the error E. If $E = \mathcal{O}((\Delta x)^n, (\Delta t)^n)$ as $\Delta x \to 0$ and $\Delta t \to 0$, the scheme is of order n in space and time.

In computational fluid dynamics, several methods are used to simulate turbulent flows. One example is the Reynolds Averaged Navier-Stokes (RANS), where the Navier-Stokes equation is averaged over time, with the turbulent velocity being $\boldsymbol{u} = \bar{\boldsymbol{u}} + \boldsymbol{u'}$. The averaging leads to RANS being time independent. As a result of the time averaging, a *turbulent shear stress*, or the Reynolds stress tensor, is introduced. This constitutes an additional term in the equations and can be modeled by means of different hypotheses and assumptions. As an example, the $k - \epsilon$ model is frequently used and based on the Boussinesq hypothesis (Chang et al., 2011 [21]), where the Reynolds stress is approximated by an algebraic equation. Here, in addition to the

usual fluid equations, transport equations for the kinetic energy k and the energy dissipation rate ϵ are solved. RANS is typically used in engineering applications, in order to minimize the numerical costs. However, due to the turbulence modeling, not all scales exhibited by the flow are resolved by RANS, only the larger scales. Some information will thereby be lost, and simulations cannot be said to be surely correct at all cases. This is the case also in a Large Eddy Simulation (LES), another commonly applied turbulence simulation method. This method is an improvement compared to RANS, as time dependence is taken into account. In RANS, one single turbulence model is used, which is not sufficient for an exact description of the flow, as small eddies behave differently from the large ones. The small ones have an isotropic nature and a universal behaviour, as discussed in section 2.4, while the behaviour of large energy-containing eddies is dependent on the geometry of the specific flow. LES takes this difference into consideration, in the sense that the large eddies are time-dependently simulated for each problem, while the behaviour of the smaller ones are captured with one model, due to their universality. The Navier-Stokes equations are spatially *filtered*, in order to eliminate the smallest length scales. Through this filtering process only the largest scales are kept and can thus be resolved time dependently. Without having to resolve all scales, the computational costs are reduced. However, as the smallest scales are only modeled and not resolved, there is still room for improvement. Therefore, when examining turbulence in a more fundamental and accurate way, like in this thesis, Direct Numerical Simulation (DNS) is used.

3.1 DNS

In DNS, the Navier-Stokes equations are basically solved with no assumptions or simplifications. Instead of statistically averaged equations, like in RANS, the equations are in DNS solved in a direct manner. The turbulent flow is in that sense regarded as any general flow. Unlike RANS and LES, there is no modeling at any scales. All spatial and temporal scales are resolved, all the way down to the Kolmogorov scale, implying a very high computational cost. This is the reason why DNS cannot be applied to most engineering problems: the range of scales is simply too wide in case of high real-life Reynolds numbers, and the computational costs become too high for computers of today to handle them. DNS becomes very costly also at moderately high Reynolds numbers. As DNS instantaneously solves for all flow variables, it gives the most precise decription of turbulence and can help building better turbulence models. Precise details of turbulence parameters,

their transport and budgets are achieved. As stated by Squires & Eaton (1990) [13], results from DNS can also provide information that cannot be obtained from experiments. It is also advantageous in the present work as the small scale turbulent vorticity may be significant for the particle behaviour, and DNS provides precise information of this. When it comes to particle-laden flows, Boivin et al. (1998) [1] point out that DNS is advantageous as the properties of the turbulence are directly available all along particle trajectories.

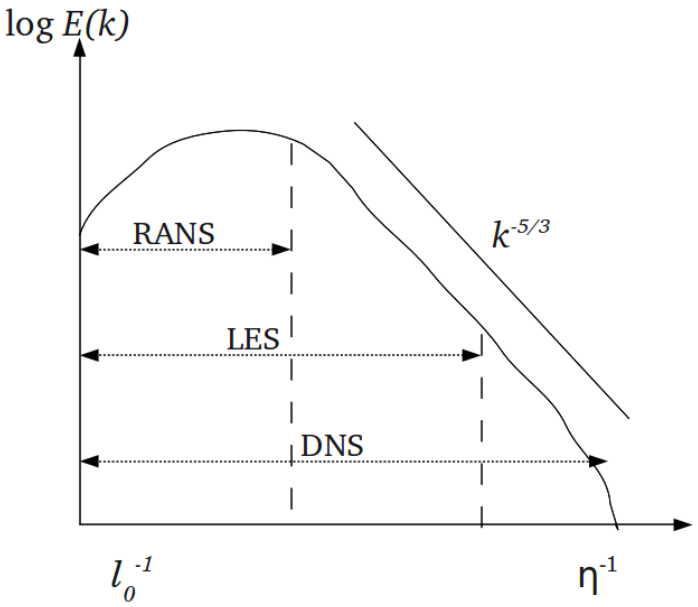

Figure 3.1: Sketch of the turbulent energy spectrum logarithmically plotted against the wavenumber k. For increasing wavenumber, the regimes in which RANS, LES and DNS work are seen. The largest length scale is l_0. The $k^{-5/3}$ proportionality is seen in the universal equilibrium range, while for low k, an arbitrary graph shape is chosen.

3.1.1 Computing costs

As previously stated, the computing costs in DNS increase rapidly with the Reynolds number. The costs are obviously also largely determined by the resolution of the simulation. The biggest DNS up to this date was done by Kaneda et al. (2003) [22] with a resolution of 4096^3, a three-dimensional domain, a box, with 4096 grid points in each direction.

Also in the present work, turbulence is created in a three-dimensional box. The size of this box has to be big enough to contain the largest turbulent eddies, which interact with and extract energy from the mean flow (Versteeg & Malalasekera, 2007 [23]). On the other hand, a small Δx is needed for the dissipative scales to be resolved. As seen before, $\mathrm{Re_c} \propto \nu^{-1}$. The mesh spacing Δx should be in the order of the Kolmogorov length η as given by (2.25), $\eta \propto \nu^{3/4}$. In order to get the smallest scales resolved, the number of meshpoints in one direction i must be

$$N_i \propto \eta^{-1} \propto \nu^{-3/4} \propto \mathrm{Re_c}^{3/4}, \tag{3.1}$$

leading to a total number of meshpoints in the order of

$$N_{3\mathrm{D}} \propto \mathrm{Re_c}^{9/4}. \tag{3.2}$$

This means that for every time step at least $N_{3\mathrm{D}}$ equations are solved. To get an appropriate value of the time step, it is noted that in order to solve all equations at all grid points, it is desired that a fluid element only move from one grid point to the next one within a single time step. Otherwise, information will be lost. To control the time step in this manner, the Courant-Friedrichs-Lewy (CFL) number c_{CFL} is introduced; it is shown by Moin & Mahesh (1998) [24] that c_{CFL} must be sufficiently low for the error to be minimized. The implementation of the CFL number for this work will be discussed in the next chapter, along with a description of the DNS code used.

Chapter 4

Numerical method

4.1 The Pencil Code

It is clear that Direct Numerical Simulations of flows with very high $\mathrm{Re_c}$ are not feasible. For simulations with feasible $\mathrm{Re_c}$, it is crucial to find a fast and accurate computer code. The DNS code used here is The Pencil Code [25], based on the finite difference method. The code is designed for running on parallel computers, using Message Passing Interface (MPI) for communication between the processors. The code deals primarily with weakly compressible turbulent flows. It is highly modular, meaning that the user can specify physics modules relevant for the specific problem. The modules solving the equations are written in `Fortran`. The code can be run on any UNIX based system with a f90 or f95 compiler. To acquire a satisfactory accuracy, the code is of sixth order in space and a third order Runge-Kutta method is used for the time integration. In The Pencil Code, equations are at all instants solved along one dimensional arrays, or 'pencils', which ensures that all information needed by the working CPU fits in the computer's cache. This is considerably faster than working on the whole domain at all instants. The CFL number, whose importance was discussed in the previous chapter,

$$c_{\mathrm{CFL}} = \frac{u_{\max}\Delta t}{\Delta x_{\min}} \tag{4.1}$$

has to be less than 1, for the code to remain stable. It is clear that with $c_{\mathrm{CFL}} > 1$, a signal covers a greater distance than $\Delta x_{\min}$ during the time Δt. The maximum speed $u_{\max} = \max(|\mathbf{u}| + c_{\mathrm{s}})$ of a fluid element is dependent on the speed of sound c_{s}, due to the compressibility of the flow. In all simulations, $c_{\mathrm{CFL}} = 0.4$ is used, and this gives a unique Δt for each iteration. The value of c_{s} is set according to the findings of Bjørnstad (2010) [11].

4.2 Boundary and initial conditions

The Pencil Code allows for different boundary conditions, like symmetric, anti-symmetric or periodic. The 2D domain containing the cylinder cross section and the surrounding flow has periodic boundary conditions in the y-direction, meaning that a particle hitting the wall at $y = 0$ or $y = L_y$ immediately is reinserted at the same x-point on the other side, with the same velocity and in the same state, cf. figure 4.3(b). Particles are inserted close to $x = 0$, a few grid cells in the direction of the fluid flow, and are removed from the simulation when hitting the cylinder or the rightmost boundary at $x = L_x$. Boundary conditions will be further discussed in later sections. The turbulence is established prior to the simulation of the fluid flow and the particle behaviour around the cylinder.

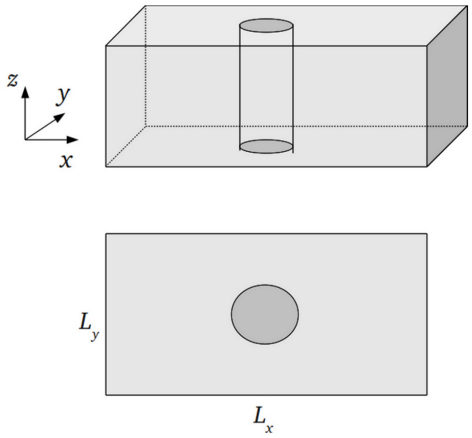

Figure 4.1: The circular cross section of the three dimensional cylinder is projected onto the two dimensional domain on which the flow is simulated.

4.2.1 The turbulent box

The simplest turbulent flows are characterized by isotropy and homogeneity. Isotropy implies that the statistical features of the turbulence have no directional preferences, i.e. the turbulence looks similar in all directions and perfect disorder reigns (Hinze, 1975 [26]). Mathematically, isotropy can be expressed by a vanishing gradient of the mean fluid velocity. Isotropic turbulence is in the present work created inside a cubic domain, the *turbulent*

box. Homogeneous and isotropic turbulence is not statistically stationary (Eswaran & Pope, 1987 [27]), as there is no energy production and thus the turbulence decays over time. Statistical stationarity is an attribute that is advantageous in the analysis of turbulence, also in particle motion examination in the present work, and the decay of turbulence complicates the understanding of e.g. particle motion (Boivin et al., 1998 [1]).

In the present work, by creating turbulence by the use of *forcing*, statistically stationary turbulence is achieved, and the above mentioned complications are avoided. Energy is added at a low wave number, i.e. large length scale, and the turbulence is developed until the energy added is equal to the energy dissipated in the high wave number range. This leads to an equilibrium where particle motion is independent of the turbulence's initial conditions (Boivin et al., 1998 [1]). The forced turbulence is basically created by adding a stochastic forcing function (as given by Haugen et al. (2004) [28])

$$\mathbf{f}(\boldsymbol{x},t) = \Re\{N\mathbf{f}_{\boldsymbol{k}(t)}\exp[i\boldsymbol{k}(t)\cdot\boldsymbol{x} + i\phi(t)]\} \tag{4.2}$$

as an external force to the right side of (2.2). As $\boldsymbol{k}(t)$ and $\phi(t)$ are chosen randomly at each time step, the stochastic nature of turbulence is inherent in the equation. The normalization factor is $N = f_0 c(|\boldsymbol{k}|c/\Delta t)^{1/2}$ and $\mathbf{f}_{\boldsymbol{k}(t)}$ is perpendicular to $\boldsymbol{k}$ and is an eigenfunction to the curl operator. In The Pencil Code, a wavenumber forcing value $|\boldsymbol{k}_\mathrm{f}| = k_\mathrm{f}$ is set. The magnitude of the randomly chosen $\boldsymbol{k}(t)$ is in the range $k_\mathrm{f} - 0.5 < |\boldsymbol{k}(t)|/k_0 < k_\mathrm{f} + 0.5$, where $k_0 = 2\pi/L_\mathrm{box}$ is the normalizing wavenumber corresponding to the side lengths L_box of the box. The effect of the forcing is that turbulent energy is put into the system at the spatial scales corresponding to the forcing wavenumber k_f, which in this manner determines the behaviour of the turbulence. As k_f is normalized by k_0, the forcing length scale will be $l_\mathrm{f} = L_\mathrm{box}/k_\mathrm{f}$.

4.2.2 The two-dimensional flow domain

Prior to letting the turbulence enter the domain, von Kármán vortices, explained in section 1.2.4, in a steady state are established in the wake of the cylinder. When this is done, the generated turbulence is used as inlet for the two dimensional domain containing the flow, the cylinder and the particles, when running a turbulent simulation. The procedure is illustrated in figure 4.2, and has been implemented in the code and tested for the present study. A quadratic xy-slice of the turbulent box is divided into strips whose velocity information is extracted and inserted at the leftmost side of the domain. Thus, it is important that the number of processors and the number of

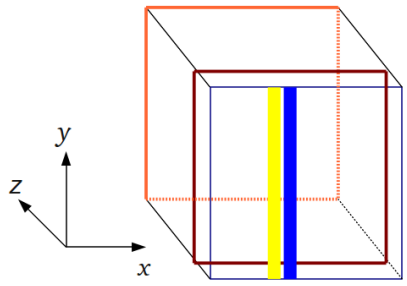

(a) Turbulent box.

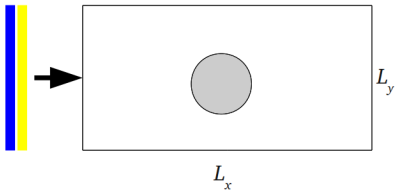

(b) Turbulent inlet on the domain.

Figure 4.2: Figure (a) shows how turbulent velocity information containing strips (yellow and blue here) at discrete increasing x-values are successively extracted from the xy-plane, i.e. for constant z. As all strips for $z = 0$ are extracted, in the blue marked plane, the procedure is repeated at next discrete z-value. When the last xy-plane, the orange one, is used, the procedure starts over again. In (b) it is shown how the turbulent velocities of the successive strips are imposed on the boundary of the domain.

grid points in the y-direction is the same for both the three dimensional turbulence generating simulation and the corresponding two dimensional flow simulation. At successive time steps, the position of the strips chosen depends on the distance traveled by the fluid, i.e. $U_0 t$. When the end of a slice is used as inlet, the slice at the next discrete z-value is used in the same manner. When the outer end of the box is used, i.e. the slice at the maximum z-value, the procedure is started over again with the strips from the slice at $z = 0$. Imposing turbulence in this way essentially means adding the turbulent velocity $\boldsymbol{u}_\mathrm{t}$ to the velocity $U_0\hat{\boldsymbol{x}}$, imposed at $x = 0$, which would be the inlet velocity in case of no turbulence. Hence, the velocity at the inlet is

$$\boldsymbol{u}_\mathrm{in} = U_0\hat{\boldsymbol{x}} + \mu_\mathrm{turb}\boldsymbol{u}_\mathrm{t}, \tag{4.3}$$

where μ_turb is a number describing the magnitude of the imposed turbulent velocity; $\mu_\mathrm{turb} > 1$ implies that the turbulent velocity fluctuations and thus u_rms in the 2D domain is increased compared to its values from the

created box turbulence. The boundary conditions implemented when imposing the turbulent velocity at $x = 0$ are called *Navier-Stokes characteristic boundary conditions* (NSCBC), and are treated by a single module in The Pencil Code. The advantage of using NSCBC is that the boundaries are non-reflecting, meaning that any signal is let through them. If they were reflecting, there would be the risk of standing waves, or numerical noise, disturbing the solution. The direct numerical simulation of compressible flows requires an accurate control of wave reflections from the domain boundaries, as the accuracy of the solution is in general sensitive to solutions at boundaries (cf. Poinsot & Lele, 1992 [29] and Lodato et al., 2008 [30]). In turbulent flow simulations, and specifically in DNS, where the range of scales is large, reflected waves can cause problems; the boundaries are 'hit' by e.g. convected vorticity and sound waves, and the reflections of these lead to oscillations being superposed with the computed solution (Lodato et al., 2008 [30]). Thus, the wrong results are obtained. The transparency of NSCBC prevents this.

The rectangular flow domain has side lengths L_x and L_y in the x and y direction respectively, with $L_x = 2L_y$. Periodic boundary conditions are imposed at the lower and upper sides of the domain, at $y = 0$ and $y = L_y$. The boundary conditions are the same for the particles as for the flow. Periodicity implies that a fluid element or a particle hitting the boundary immediately reappears in the same state with the same velocity at the opposite side.

4.2.2.1 Ghost points and the solid cylinder

Numerically, the boundary conditions are taken care of by the use of *ghost points*, quasi virtual grid points, outside the domain. The domain is represented by a grid with n_x points in the x-direction and n_y in y. At each side of the grid points in each dimension, three ghost points are added. Depending on which boundary conditions are used, values at the six ghost points in each direction are set equal to the values calculated at the corresponding grid points, cf. figure 4.3. In this way, a symmetric boundary condition can be imposed by setting the same value to both the grid point and the ghost point nearest, but on opposite sides of a boundary. As three ghost points are present at each boundary, any grid point will have three nearest neighbours on each side along each pencil, i.e. in each dimension. Thus, the boundary conditions are sufficient for sixth-order spatial differences.

The position of the cylinder is in the middle of the domain. The cylinder, being a solid geometry, is modeled using the *immersed boundary method* described by Haugen & Kragset (2010) [4]. With this method, a grid of ghost points is used within the cylinder area, such that imposed boundary conditions represent a distinct wall between the cylinder and the flow domain.

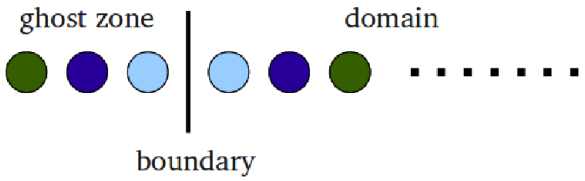

(a) Symmetric boundary conditions.

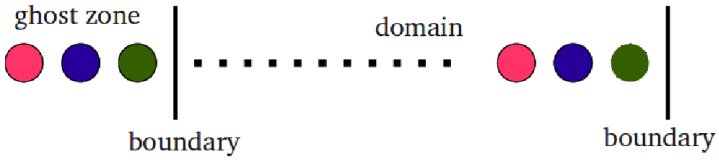

(b) Periodic boundary conditions.

Figure 4.3: Ghost points are assigned values according to the calculated values at corresponding points, i.e. points with the same colour, in the domain. In the case of antisymmetric boundary conditions, the values assigned to the ghost points shown in figure (a) would be of the opposite sign of the corresponding points in the domain.

Values at one of these ghost points are chosen according to the corresponding *mirror point*, a point within the fluid domain grid which is found by mirroring the ghost point across a symmetry line parallel to the tangent of the curved cylinder. Interpolation between mirror point neighboring grid points is needed for calculating the values at the mirror point, as it will not necessarily be a grid point.

4.3 The particles

4.3.1 One-way coupling

As the focus is particle transport in turbulence, i.e. the impact of the turbulence on the particles, *one-way coupling* is assumed. This implies that the effect of the velocity field of the fluid affects the particles, but not the other way around. This is already seen from the expression for the drag force (2.8); the fluid velocity $\boldsymbol{u}$ is contributing to the particle motion. This one-way coupling is the typical method when considering only particle transport, while by two-way coupling also the modification of turbulence from higher mass loadings of particles is studied (Maxey et al., 1997 [31]). One-way coupling

implies that the turbulence behaves as if there were no particles present, and the intensity of the turbulence is not lowered, as can be the case in a similar real-flow scenario. However, the assumption is valid, since it is knowledge of the particle behavior resulting from the presence of turbulence that is the goal of this work. As pointed out earlier, a low particle to fluid density ratio also makes one-way coupling reasonable.

4.3.2 Inserting particles

Among similar simulations done in the past, there have been some disagreements related to the correct number of particles to insert to achieve the desired statistical reliability of the data (Strutt et al., 2011 [32]). Therefore, a large number of particles, $N = 10^6$, is inserted in each simulation. When the turbulence has fully entered the domain and the statistically steady state has been reached, particles are released a few cells downstream at the leftmost edge. If they are deposited at the cylinder or reach the rightmost edge of the domain, they are removed from the simulation. The particles are inserted continuously over a time interval corresponding to multiple Von Kármán eddy periods, controlled by the particle insertion rate r_{insert}. Inserting particles at the farthest edge upstream of the cylinder is necessary for the particles to interact with the flow velocity and be distributed dependent on the flow structure and thereby to achieve a more physical realization of the system. The initial velocity of the particles is equal to the mean flow of the fluid, $U_0\hat{\boldsymbol{x}}$, and the width $l_{\text{par,run}}$, the y range over which the particle cluster is inserted is set such that it at least spans the cylinder diameter D. The width $l_{\text{par,run}}$ can be adjusted in the different runs, depending on the k_f used. Particles inserted in the domain at an unnecessarily large $|y|$-position will only increase computational cost, and not give any better deposition statistics (Bjørnstad, 2010 [11]). However, it is essential that $l_{\text{par,run}}$ is at least as large as the largest turbulent eddies, because particles change velocity direction when being influenced by the eddies, and will thus be captured even though they were not inserted in front of the cylinder. In the laminar cases, it is sufficient with $l_{\text{par,run}} = D$, as the particle paths follow the laminar streamlines perfectly and thus go straight in the x direction.

4.3.3 Capture efficiency

If in total N particles are inserted, then $N_{\text{init}} = N\frac{D}{l_{\text{par,run}}}$ initially start right in front of the cylinder. When N_{cap} particles are captured, this gives the

capture efficiency

$$\eta = \frac{N_{\text{cap}}}{N_{\text{init}}} = \frac{l_{\text{par,run}}}{D}\frac{N_{\text{cap}}}{N}. \tag{4.4}$$

As the particles with largest St are awaited to easily be captured because of their large inertia, a lower number of these particles is needed, than number of particles with smaller St, to achieve statistically significant results. Likewise, a high number out of the total N particles have small St, because of the much lower probability for these particles to be captured. In the present work, all particles that hit the cylinder are captured. This implies that all particles stick to the cylinder surface, which would not necessarily be the case in a real-world scenario. The conditions under which particles will stick to a cylinder surface are studied by Wang (1986) [33] and Rosner & Tandon (1995) [34].

Here, *capture* is the same as *deposition*, used previously. Capture efficiency thus quantifies the deposition of particles. When presenting and discussion the results, in the remaining part of the thesis, *capture* will primarily be used.

Chapter 5

Results and discussion

In this chapter, results from the simulations are presented. This includes mainly capture efficiency curves both at $\mathrm{Re_c} = 421$ and $\mathrm{Re_c} = 1685$, compared between different forced cases with turbulence and laminar reference cases. Values of parameters used in the simulations are given in appendix B. The 2D domain had the same physical size at both $\mathrm{Re_c}$. The simulations with $\mathrm{Re_c} = 421$ were run on a domain with 1024 grid points in the x-direction and 512 grid points in the y-direction, while the $\mathrm{Re_c} = 1685$ simulations were run with 2048 and 1024 grid points in the respective directions. The 3D box simulations of turbulence were run with resolutions 512^3 and 1024^3 for $\mathrm{Re_c} = 421$ and $\mathrm{Re_c} = 1685$ respectively. The need for accurately resolving the boundary layer of the cylinder is the strictest resolution requirement in the simulations. As the thickness of the boundary layer scales as $\delta_{\mathrm{layer}} \propto 1/\sqrt{\mathrm{Re_c}}$, a Reynolds number of 1685 requires doubled resolution in every direction in order to resolve the boundary layer, compared to what is required for the four times lower $\mathrm{Re_c} = 421$.

The turbulent pre-simulations are shortly discussed in section 5.1. The deposition of particles on the cylinder, expressed by the capture efficiency, is presented thereafter. In section 5.2, the results from the $\mathrm{Re_c} = 421$ simulations are presented. The $\mathrm{Re_c} = 1685$ results are given in section 5.3, which is followed by a discussion on comparing observations on the differences between the simulations at the two Reynolds numbers. This also includes the results of backside impaction, particles colliding with the backside of the cylinder. Particle clustering is treated in section 5.5. A discussion on how the vorticity plays a role concludes the chapter.

In figure 5.1, the *frontside* and *backside* of the cylinder is illustrated. The deposition of particles mainly takes place on the frontside of the cylinder. Thus, the major emphasis is put on the results of the frontside capture effi-

ciency η. However, some backside capture is found, but is only considered in section 5.4.2. Backside capture will be denoted by η_{back}.

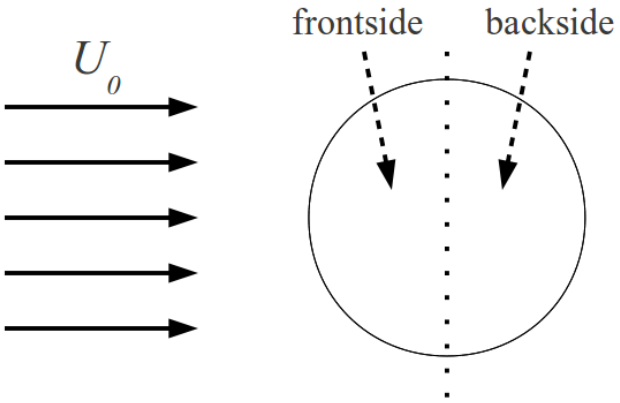

Figure 5.1: The frontside and backside of the cylinder. The fluid flows towards the cylinder with mean velocity U_0.

5.1 Simulations of turbulence in 3D

The goal of the 3D pre-simulations of turbulence was to establish homogeneous, statistically stationary conditions. Stationarity in the turbulence implies that the stochastic fluctuations reach a steady state, i.e. u_{rms} stays constant in time. For both Reynolds numbers, three different turbulent forcing scales were applied, i.e. three turbulent boxes simulated for each Reynolds number. Table 5.1 lists values of u_{rms} achieved in the simulations of turbulence. Small length scale forcing corresponds to a forcing wavenumber $k_{\text{f}} = 15$, intermediate scale to $k_{\text{f}} = 5$, while $k_{\text{f}} = 1.5$ corresponds to large scale forcing. The shape of the energy spectrum in figure 5.2 is seen to correspond with the general trends described in section 2.4, even if the Reynolds number is too low for the characteristic $E(k) \propto k^{-5/3}$ shape in the universal equilibrium range to be present.

Table 5.1: Values of u_{rms} for all the turbulence simulations, given in m/s. The product $u_{\mathrm{rms}}k_{\mathrm{f}}$ becomes useful later, as it expresses the magnitude of vorticity.

	k_{f}	u_{rms}	$u_{\mathrm{rms}}k_{\mathrm{f}}$
$\mathrm{Re_c} = 421$	15	0.8637	12.956
	5	1.337	6.685
	1.5	2.117	3.176
$\mathrm{Re_c} = 1685$	15	1.191	17.865
	5	1.404	7.02
	1.5	1.473	2.21

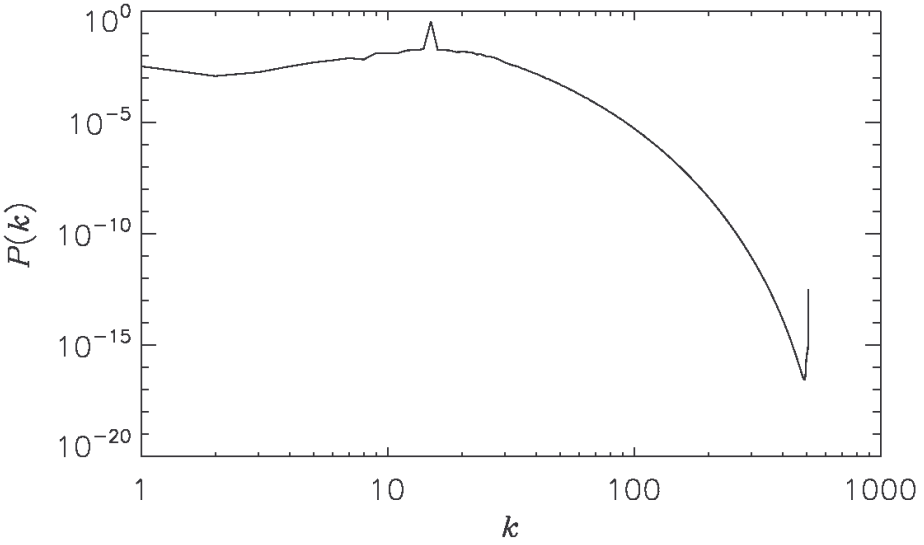

Figure 5.2: Power spectrum of turbulent kinetic energy. The turbulence was run at $\mathrm{Re_c} = 1685$ and forced at $k_{\mathrm{f}} = 15$, which is seen in the peak in energy at $k = 15$. The energy is well dissipated for high wavenumbers, where the irregularity at the highest wavenumber is due to the numerics.

5.2 Simulations with $\mathrm{Re_c} = 421$

Figure 5.3 shows the capture efficiencies, as function of the Stokes number, resulting from the four cases L1-L4, as given in table 5.2. The typical shape is as seen in the literature, e.g. Guha (2008) [7] and Haugen & Kragset (2010) [4]. As described in the latter of these, three modes are found in the plotted capture efficiency, namely the inertial impaction mode, the boundary stop-

Table 5.2: Overview of the 2D simulations. In the column CASE, 'L' corresponds to lower resolution runs and 'H' to higher.

CASE	RESOLUTION	$\mathrm{Re_c}$	FLOW REGIME	μ_{turb}
L1	1024×512	421	Laminar	$\cdots$
L2	1024×512	421	Turbulent; $k_{\mathrm{f}} = 15$	1.0
L3	1024×512	421	Turbulent; $k_{\mathrm{f}} = 5$	1.0
L4	1024×512	421	Turbulent; $k_{\mathrm{f}} = 1.5$	1.0
H1	2048×1024	1685	Laminar	$\cdots$
H2	2048×1024	1685	Turbulent; $k_{\mathrm{f}} = 15$	1.0
H3	2048×1024	1685	Turbulent; $k_{\mathrm{f}} = 5$	1.0
H4	2048×1024	1685	Turbulent; $k_{\mathrm{f}} = 1.5$	1.0
H5	2048×1024	1685	Turbulent; $k_{\mathrm{f}} = 15$	1.5
H6	2048×1024	1685	Turbulent; $k_{\mathrm{f}} = 5$	1.5
H7	2048×1024	1685	Turbulent; $k_{\mathrm{f}} = 1.5$	1.5
H8	2048×1024	1685	Turbulent; $k_{\mathrm{f}} = 15$	2.0
H9	2048×1024	1685	Turbulent; $k_{\mathrm{f}} = 5$	2.0
H10	2048×1024	1685	Turbulent; $k_{\mathrm{f}} = 1.5$	2.0

ping mode and the boundary interception mode. In the following sections, these modes are identified according to the plotted capture efficiencies.

5.2.1 Inertial impaction mode

The *inertial impaction mode* is found for the region $\mathrm{St} \gtrsim 0.5$ for all four simulation cases. This inertial impaction mode found for the largest particles is also described by Douglas & Ilias (1988) [8]. It arises due to the large inertia of the particles in this mode; they are barely affected by the fluid flow, and it is thus awaited that the presence of turbulence does not lead to any significant change in capture. This presumption is verified by in the present work. The initial velocities of the particles are maintained and thus the deposition is large; the particles starting in front of the cylinder stay in front of the cylinder, and are to little extent affected by the boundary layer.

5.2.2 Boundary stopping mode

When the Stokes number decreases from $\mathrm{St} = 0.50$, the capture efficiency falls steeper than it does for decreasing Stokes numbers in the inertial impaction mode. This is in agreement with Bjørnstad [11] and Haugen & Kragset [4].

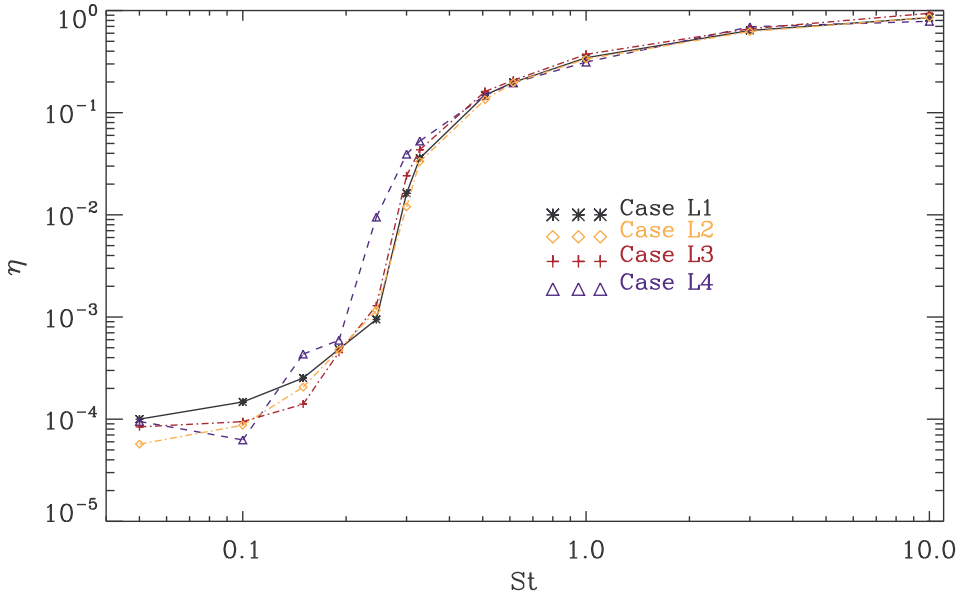

Figure 5.3: The frontside capture efficiency η plotted against the Stokes number St at Re_c=421.

The simulations ran in the latter study are only laminar, and the capture efficiency's dependence on the Reynolds number is studied. However, both $Re_c = 421$ and $Re_c = 1685$ are covered, so the achievements of the study are comparable to the laminar results of this work. The important *boundary stopping mode* in the range $0.15 \lesssim St \lesssim 0.5$ is where the interesting results are mainly found. The mode appears after a gradual transition from the inertial impaction mode and into this region with the more declining capture efficiency for decreasing Stokes numbers below 0.5. The lower limit for this region, at $St \approx 0.15$, correlates well with the what was found by Haugen & Kragset (2010) [4] and Bjørnstad (2010) [11]. At this Stokes number and below, the particles start lacking the inertia needed to penetrate the boundary layer of the cylinder. As is shown by Haugen & Kragset (2010) [4], the lower Stokes number limit for the boundary stopping mode depends on the Reynolds number. This reflects the fact that the boundary layer characteristics, e.g. its thickness, depend on the viscosity. The capture efficiency's strong dependence on a change in the Stokes number is the characteristic attribute of this mode.

5.2.3 Boundary interception mode

For St $\lesssim 0.15$, the *boundary interception mode* is found. It is seen that η is again less dependent on St, meaning that the curve is consistently flattening for decreasing St. In the boundary interception mode, the particles have such a low inertia that they follow the fluid almost perfectly. Still, the impaction rate is not zero. The particles are impacting due to them being physical particles with finite radii, and some of them are therefore able to get close enough to hit the cylinder. Haugen & Kragset (2010) [4] investigate which and where particles are deposited by considering the laminar boundary layer thickness, which is varying with position around the cylinder surface. In this way, Haugen & Kragset (2010) [4] find where on the cylinder the particles with the lowest Stokes numbers most likely will deposit, by looking how their radial velocity towards the cylinder varies due to the varying boundary layer thickness. This leads to an angle dependent deposition distribution around the cylinder frontside.

Looking at figure 5.3, it can be said that this mode for case L4 is shifted somewhat to the left compared to L2 and L3, due to the higher capture at both St = 0.15 and St = 0.19. In general, as few particles are captured in the boundary interception mode, statistical deviations may as stated give the results less confidence. The turbulent capture efficiencies in this mode will also be discussed in chapter 6.

5.2.4 The effect of turbulence on the capture efficiency

For easier to study the effects of the turbulence, the relative differences

$$\delta_{\text{Case}} = \frac{\eta_{\text{Case}} - \eta_{\text{laminar}}}{\eta_{\text{laminar}}} \tag{5.1}$$

between capture efficiencies in the different turbulent cases and the laminar are plotted. A negative δ_{Case} thus implies a larger capture in the laminar case. For $\text{Re}_c = 421$, the respective relative differences for L2 through L4 versus the laminar L1 are plotted in figure 5.4.

Bjørnstad's (2010) [11] study also contains a laminar reference case and 2D turbulent simulations forced at $k_f = 1.5$ and $k_f = 5$ respectively. In the inertial impaction mode, the general trend is, as previously stated, that the turbulent η's do not deviate much from the laminar. Bjørnstad's (2010) [11] findings support this. However, not any major differences between turbulent and laminar cases are expected in this mode.

From the lower region of the boundary stopping mode and upwards, the capture efficiency for case L4 obtains the highest values. The trend is that

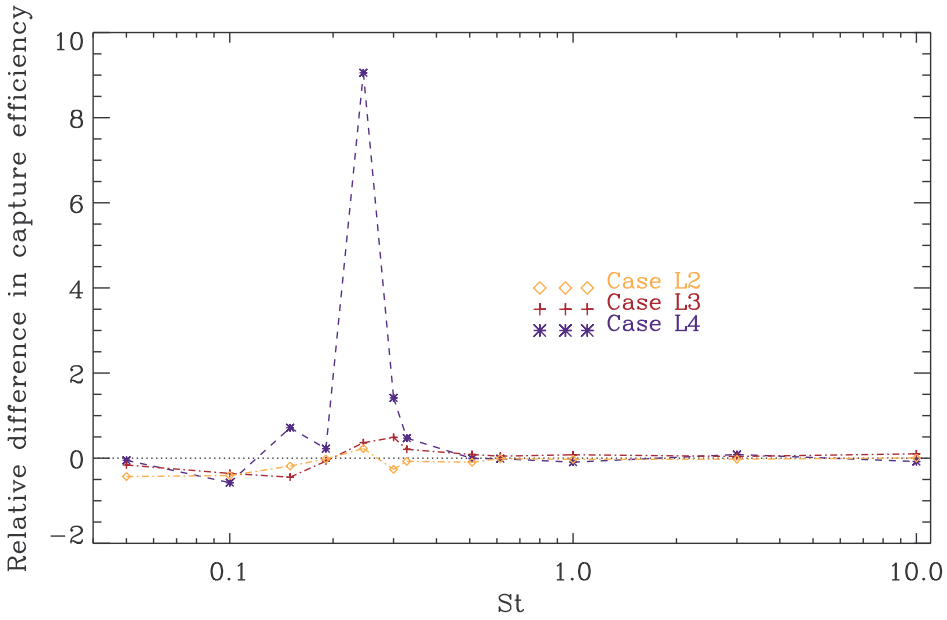

Figure 5.4: Frontside capture efficiencies at Re_c=421, shown as relative difference δ_{Case} between the turbulent cases the laminar reference case.

lowering the forcing length scale, i.e. raising k_f, yields lowered capture efficiencies. Thus, a higher δ_{L3} than achieved in the present results would be expected, as δ_{L4} attains such high values in this mode. This is the case in the results of Bjørnstad (2010) [11]; his $k_f = 5$ simulations show higher capture than the present simulations do. For the low-scale forced case L2, there is only a smaller region approximately with $St \in \langle 0.2, 0.25 \rangle$ where the capture efficiency is increased compared to laminar flow. For lower Stokes numbers, the relative difference in capture efficiency for the cases L2 and L3 stays slightly below zero. For higher Stokes numbers, especially in the inertial impaction mode, it is approximately zero for all cases.

In the boundary interception mode, the behaviour of the particles in case L3 is the same as found by Bjørnstad (2010) [11], namely a lower η than in the laminar case, which is the result also in case L2. For the large scale forced case what looks like random jumps are seen in δ_{L4}, indicating the less predictable η behaviour for the lowest St.

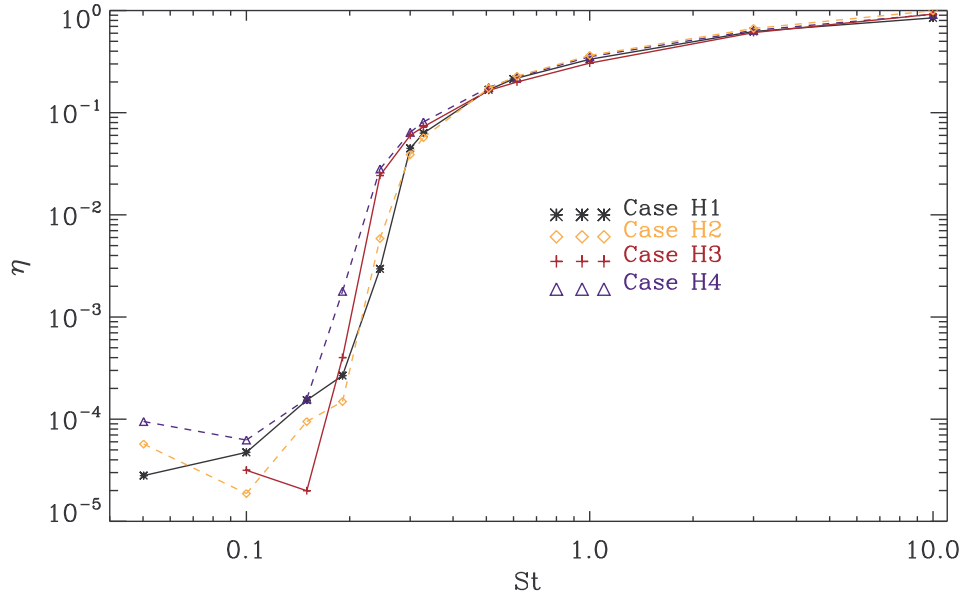

Figure 5.5: Frontside capture efficiencies at $\mathrm{Re_c}$=1685, for the laminar reference case H1 and the three turbulent forced simulations, where all three cases have turbulent velocity magnitude $\mu_{\mathrm{turb}} = 1.0$.

5.3 Simulations with $\mathrm{Re_c} = 1685$

The high resolution simulations with $\mathrm{Re_c} = 1685$ (cases H1-H10 in table 5.2) were run with inlet turbulence simulated on a 1024^3 domain. Different turbulence intensities were implemented by increased turbulent inlet velocity, i.e. altering of μ_{turb} in (4.3). The NSCBC parameters had to be adjusted carefully to avoid code crashes as the velocity of the turbulent eddies became higher. The differences in frontside capture efficiencies due to this altering of the turbulent velocities are studied in this section.

Figure 5.5 shows, in the same manner as figure 5.3, the frontside capture efficiency plots, with their characteristic shape. The boundary stopping mode can again be said to be in the domain $0.15 \lesssim \mathrm{St} \lesssim 0.5$, with the inertial impaction and boundary interception modes above and below this, respectively. No particles of the smallest size have been captured in the $k_{\mathrm{f}} = 5$ turbulence case H3. The number of particles captured is in all cases low in this region. Thus, this result is within the statistical deviation of the simulation. Like in some of the $\mathrm{Re_c} = 421$ results, the frontside capture efficiencies in the cases with turbulence have jumps for the lowest Stokes numbers, compared

to the laminar, which has a monotonically increasing capture efficiency for increasing Stokes numbers. The jumps may be due to the fluctuating eddies influencing the capture. A further discussion is given in chapter 6.

5.3.1 The impact of turbulence

In the following, the effects of turbulence at $\mathrm{Re_c} = 1685$, by means of the different forcing wave numbers k_f and increasing turbulent velocity magnitude μ_turb, are investigated by examining the plotted relative differences in frontside capture efficiency. It proved difficult to apply turbulent inlet magnitude significantly larger than $\mu_\mathrm{turb} = 2.0$, as it caused excess of numerical reflections at the boundaries and thus code crash.

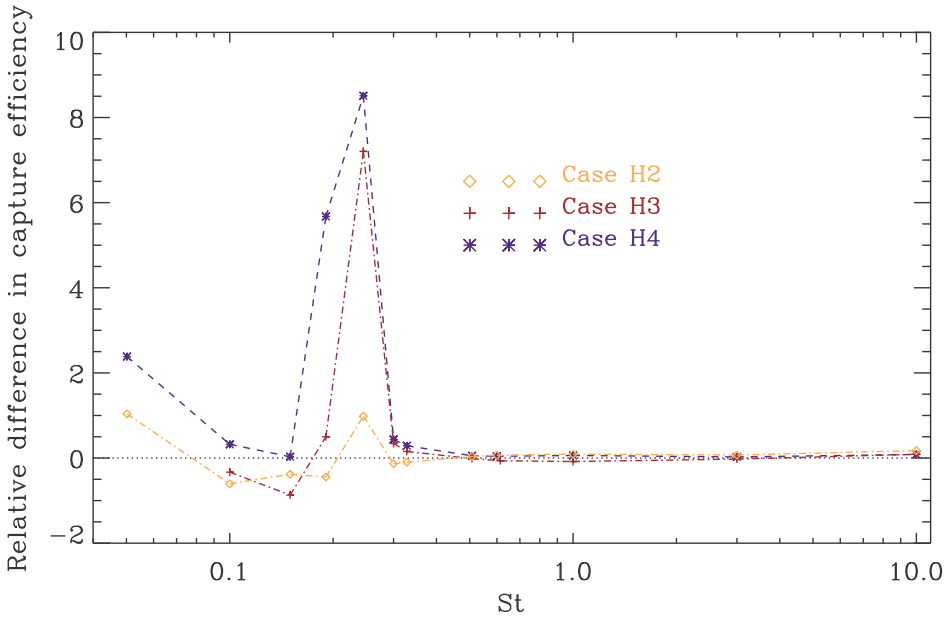

Figure 5.6: Frontside capture efficiencies with $\mathrm{Re_c} = 1685$ and $\mu_\mathrm{turb} = 1.0$, turbulent results shown as relative difference to the laminar reference case H1.

5.3.1.1 Turbulent velocity magnitude $\mu_\mathrm{turb} = 1.0$

The relative differences in capture efficiency with $\mathrm{Re_c} = 1685$ without amplification of the turbulence, i.e. with $\mu_\mathrm{turb} = 1.0$, are plotted in figure 5.6. In the boundary stopping mode, from $\mathrm{St} \approx 0.15$ and upwards, the relative differences for all cases are monotonically increasing, until the peak is

reached. The peak in relative difference is clear for all three cases, and found at St = 0.24. So the effect of turbulence is at largest in the lower region of the boundary stopping mode. The increase in η is as expected more dramatic the larger the forcing length scale is, thus the lower k_f is. At the peak, δ_{H4} is almost nine times δ_{H2}. Furthermore, the $k_f = 1.5$ turbulence capture of particles with St = 0.15 is almost ten times the laminar capture. Case H3, with $k_f = 5$, also has a dramatic increase in capture, compared to the laminar, from St ≈ 0.5 on, while the change is much less for case H2. It is also noted that the effect of the turbulence is found at the same Stokes numbers for all forcing scales.

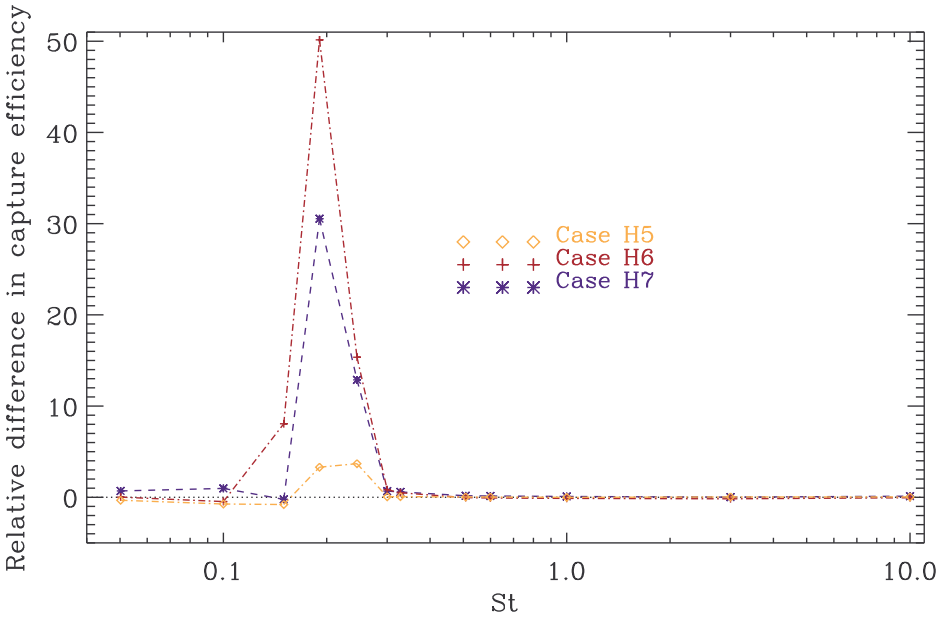

Figure 5.7: Relative differences in frontside capture efficiencies for the turbulent cases with $Re_c = 1685$ and $\mu_{turb} = 1.5$. The highest value, slightly above 50, is no shown.

5.3.1.2 Turbulent velocity magnitude $\mu_{turb} = 1.5$

When the turbulent inlet velocity is increased, the effect of the turbulence is found to be dramatically stronger. The peak in the relative difference is found at St = 0.19, cf. figure 5.7. This largest value of the relative difference, at round 50, is found in the intermediate scale forced case H6, with the large scale capture being smaller. This as opposed to the simulations with $\mu_{turb} = 1.0$, where the relative capture increases with the forcing scale

applied, which is the expected result. Interestingly, δ_{H7} is around zero at St = 0.15, even if the corresponding case H4 with $\mu_{turb} = 1.0$ was around 9. As seen in figure 5.7, the relative capture then increases rapidly from around zero to approximately 30 at St = 0.19 for this case. So all peaks are shifted somewhat to the left, compared to figure 5.6. The peak in the low scale forced case H5 is broader, compared to its height, than the other two. The inertial impaction range mode is still found in the same range; amplified velocity magnitude does not lead to increase in capture differences here. The capture for $k_f = 5$ being larger than $k_f = 1.5$ is an anomaly indicating that the implementation of $\mu_{turb} = 1.5$ might have gone wrong. However, the results confirm the trend of dramatically higher capture efficiency for increasing μ_{turb}.

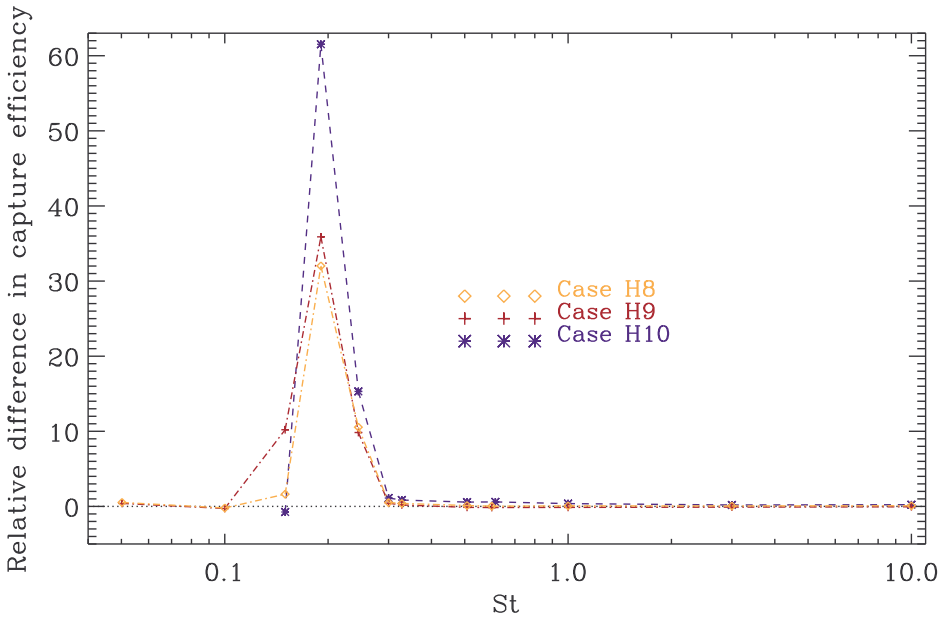

Figure 5.8: Relative differences in frontside capture efficiencies for the turbulent cases with $Re_c = 1685$ and $\mu_{turb} = 2.0$. The highest value, slighty above 50, is not shown,

5.3.1.3 Turbulent velocity magnitude $\mu_{turb} = 2.0$

The trend with strongly increasing relative capture efficiency for increasing turbulence intensity continues as the velocity magnitude is raised to $\mu_{turb} = 2.0$, as shown in figure 5.8. The results are more as expected, with increasing capture efficiency with increasing forcing scale. There is no capture at the

two lowest Stokes numbers investigated for the large scale forced case H10, while the capture for this case is slightly below the laminar at St = 0.15 and increases suddenly to above 50 times the laminar for St = 0.19. A decrease is found for the intermediate scale forced case H9, compared to what is seen in figure 5.7: The relative difference in frontside capture efficiency in case H9 is about 70 % of its value in the corresponding case H6 with $\mu_{\text{turb}} = 1.5$. Furthermore, the cases H8 and H9 have their peaks at approximately the same value of the relative; the lower scale forced case H8 peaks at about 90 % of the top value of case H9. The general trend seems to be that the effects of the differently forced turbulence converge towards each other as μ_{turb} is raised, and forcing scales becomes less important.

5.4 The effect of increased Reynolds number

The particle-laden flow has been simulated at two Reynolds numbers both at laminar conditions and at three turbulent forcing scales. In the following, major differences between the results for the two Re_c will be presented and briefly discussed. As a whole, capture efficiencies in the boundary stopping mode are found to be higher for $\text{Re}_\text{c} = 1685$ than for $\text{Re}_\text{c} = 421$.

5.4.1 Frontside capture

In the figures 5.9 and 5.10, the different frontside capture efficiencies for the two Reynolds numbers are plotted for comparison. All turbulent cases in these figures are simulated with $\mu_{\text{turb}} = 1.0$. It is seen that in the boundary interception mode, the capture efficiency for $\text{Re}_\text{c} = 1685$ is in general lower than for $\text{Re}_\text{c} = 421$. This is because the frontside capture efficiency for these lowest Stokes numbers is entirely depending on the particle radius r_p, which in the $\text{Re}_\text{c} = 1685$ cases are set to be the half of their value in the $\text{Re}_\text{c} = 421$ cases, in order to apply the same Stokes numbers for both Reynolds numbers. This is because $\text{St} \propto 1/\nu$ and $\text{St} \propto r_\text{p}^2$, cf. (2.15)*.

In all figures, the capture for the $\text{Re}_\text{c} = 1685$ simulations exceeds the capture for the $\text{Re}_\text{c} = 421$ simulations at around $\text{St} \approx 0.20$, in the lower region of the boundary stopping mode. Considering figure 5.9, in the boundary stopping mode, the difference in η between the two Re_c seems to be larger when turbulence is present, i.e. in figure 5.9(b). The plots of the laminar results, in figure 5.9(a) coincides with the results of Haugen & Kragset (2010) [4], where simulations were run at the same Reynolds numbers as here.

*The kinematic viscosity ν in the $\text{Re}_\text{c} = 1685$ simulations is one fourth of its value in the $\text{Re}_\text{c} = 421$ cases.

From around St ≈ 0.5 and onwards, the capture at both $\mathrm{Re_c}$ is much the same in all plots in both figures 5.9 and 5.10. Small differences between the $\mathrm{Re_c} = 421$ and the $\mathrm{Re_c} = 1685$ simulations are probably anomalies due to the low number of particles released within the highest Stokes numbers, and thus poor reliability in the data.

Regarding the $k_\mathrm{f} = 1.5$ simulations in figure 5.10(b), the value of the $\mathrm{Re_c} = 1685$ capture efficiency is three times larger than the $\mathrm{Re_c} = 421$ capture efficiency already at St $= 0.19$. Also, the capture is higher for the $\mathrm{Re_c} = 1685$ run throughout the whole St range except at St $= 0.15$. It can be concluded that St $= 0.15$ is within the boundary interception mode, as all $\mathrm{Re_c} = 1685$ η's are considerably smaller than the η's for $\mathrm{Re_c} = 421$. As already stated, this is because the particle radii are smaller in the $\mathrm{Re_c} = 1685$ simulations, and the finite radiues is the parameter determining the capture in this mode. Furthermore, in the laminar and low scale forced cases in figures 5.9(a) and (b) respectively, the $\mathrm{Re_c} = 1685$ capture is lower than the $\mathrm{Re_c} = 421$ capture also at St $= 0.19$. For these cases, it may be said that St $= 0.19$ is found in the boundary interception mode.

Another feature is the slightly increased capture for the lowest Stokes number for which there is non-zero capture, compared to the second lowest, in the turbulent $\mathrm{Re_c} = 1685$ cases in figures 5.9(b) and 5.10. This can indicate some unknown mechanism in this lower region of the boundary interception mode, further considered in chapter 6.

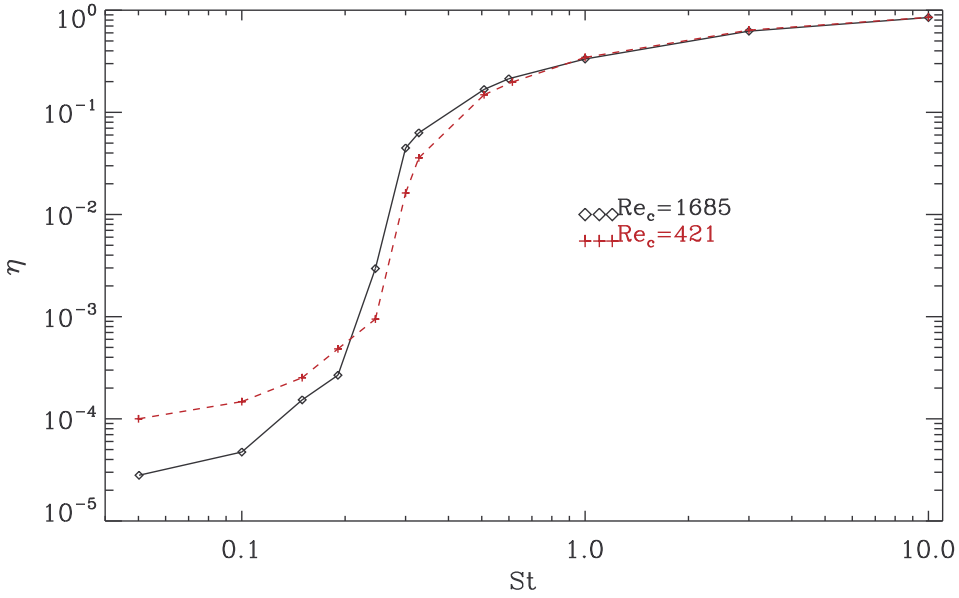

(a) Laminar cases: Case L1 with $\mathrm{Re_c} = 421$ and case H1 with $\mathrm{Re_c} = 1685$.

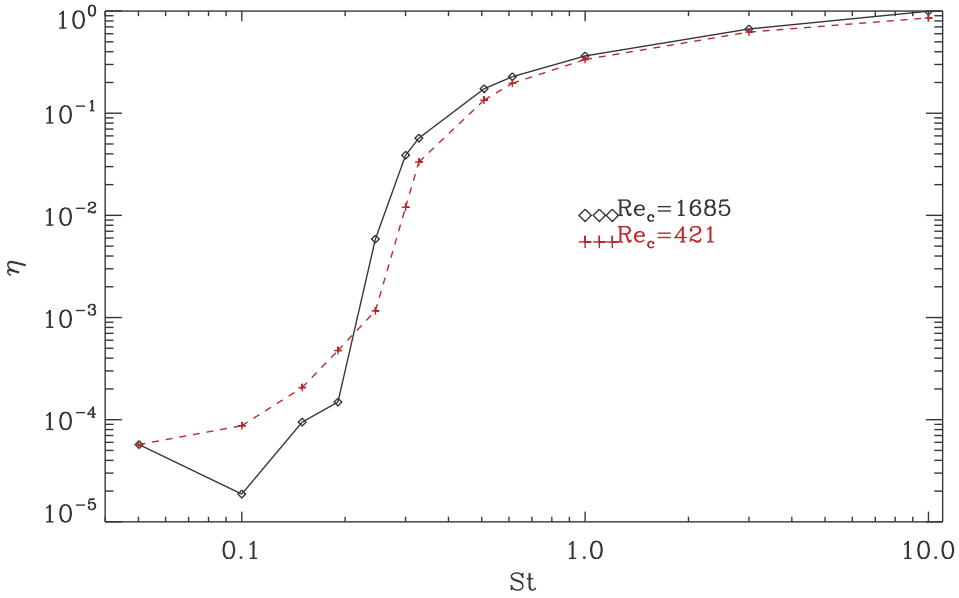

(b) Turbulent cases L2 and H2, with $k_\mathrm{f} = 15$

Figure 5.9: Frontside capture efficiencies for both $\mathrm{Re_c} = 421$ and $\mathrm{Re_c} = 1685$.

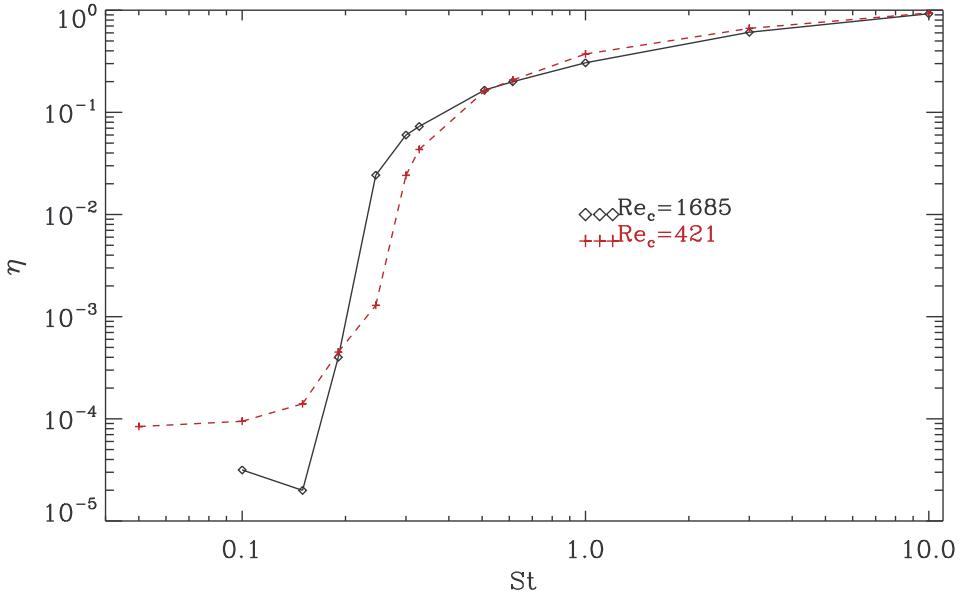

(a) Turbulent cases L3 and H3, with $k_f = 5$

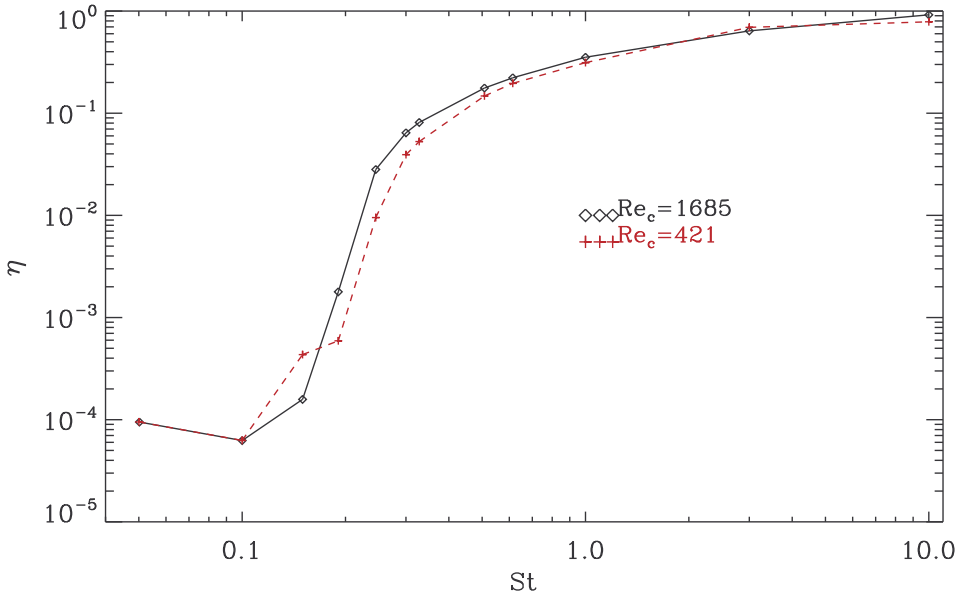

(b) Turbulent cases L4 and H4, with $k_f = 1.5$

Figure 5.10: Frontside capture efficiencies for the two larger turbulent forced cases both for $\mathrm{Re_c} = 421$ and $\mathrm{Re_c} = 1685$.

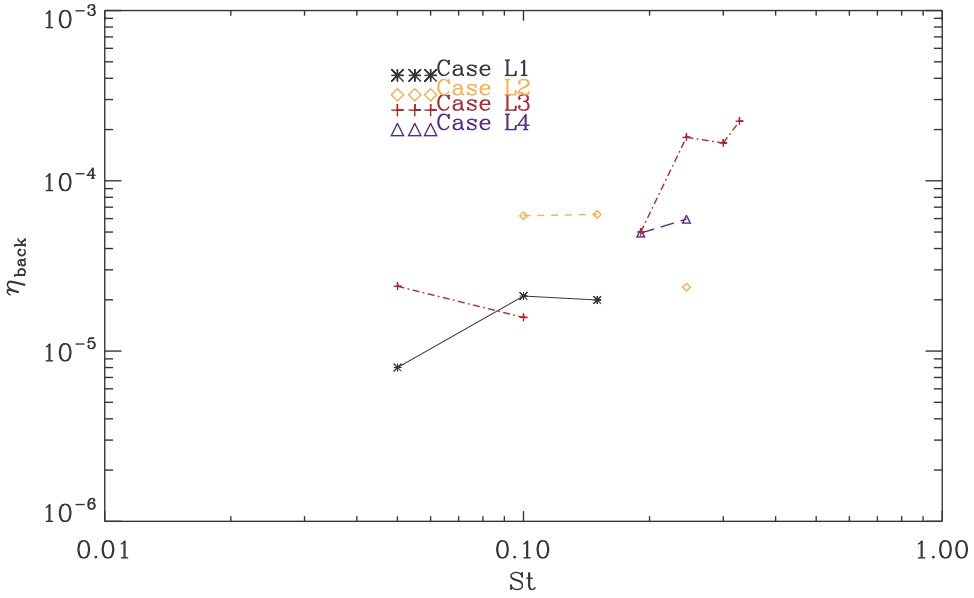

Figure 5.11: The backside capture efficiencies for all simulations with $\mathrm{Re_c} = 421$. The continuity in lines connecting the data points is broken when there exists particle sizes, for which there is no capture. The range in St for which there is capture is thus abrupted at certain points.

5.4.2 Backside capture

To further investigate the effects of the turbulent eddies on the particles, the capture on the backside of the cylinder, η_{back}, is also calculated by means of (4.4), with N_{cap} now being the number of particles captured on the backside.

In figure 5.11, the backside capture η_{back} for the $\mathrm{Re_c} = 421$ simulations is plotted. It is seen that the values for η_{back} are very low. The characteristic shape seen in the plots of the frontside capture efficiency is not present; there is only a minor capture and it takes place in the lower Stokes number range. As seen in figure 5.11, capture seems to be somewhat higher in the turbulent cases L2-L4 than in the laminar L1. The medium scaled turbulent case (L3) has the highest backside capture efficiency; capture takes place for six particle sizes and over the largest St range, namely at all Stokes numbers from $\mathrm{St} = 0.05$ to $\mathrm{St} = 0.328$, except at $\mathrm{St} = 0.15$.

It is illustrative to see how the backside capture has increased in the higher $\mathrm{Re_c}$ cases, results of which are plotted in figures 5.12 and 5.13. For the $\mathrm{Re_c} = 421$ cases, few distinct trends can be observed. However, when

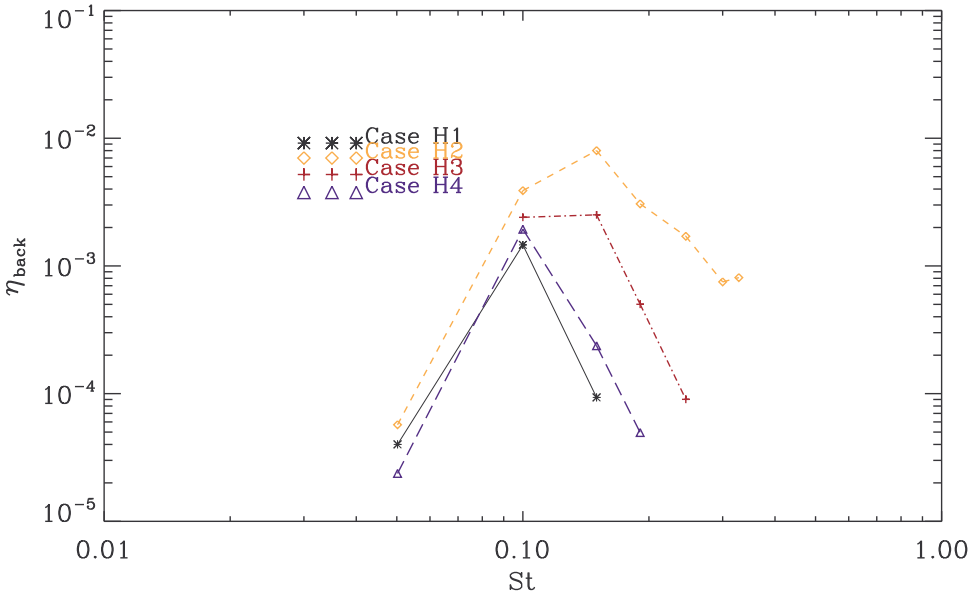

Figure 5.12: Values of the backside capture efficiency in the $\mathrm{Re_c} = 1685$ simulations with turbulent velocity magnitude $\mu_{\mathrm{turb}} = 1.0$.

the Reynolds number is raised, some general trends in the backside capture are seen. A higher capture is found at $\mathrm{Re_c} = 1685$ for all Stokes numbers in almost all cases. This becomes clearer when looking at the values given in table 5.3. Since the data is more reliable, only the $\mathrm{Re_c} = 1685$ values are considered when discussing trends. In some cases, the backside capture is larger than the frontside capture for $\mathrm{St} \lesssim 0.19$. For $\mathrm{Re_c} = 1685$, the backside capture spans across a larger interval of values than it does for $\mathrm{Re_c} = 421$; all point-connecting lines are continuous in the figures 5.12 and 5.13, implying capture for all Stokes numbers in the capture range, which for example in case H9 goes from $\mathrm{St} = 0.05$ to $\mathrm{St} = 0.60$. Also, the lowest non-zero capture for all respective cases is found at the lowest Stokes numbers for $\mathrm{Re_c} = 1685$, while for $\mathrm{Re_c} = 421$ it is more random where the capture is at its highest or lowest in the different cases. The general behaviour for the $\mathrm{Re_c} = 1685$ cases is that η_{back} increases from its initial minimum until it reaches the maximum at $\mathrm{St} = 0.15$ (or $\mathrm{St} = 0.19$ for cases H8 and H9), from which it decays.

The backside capture comes into play when particles gain inertia from the eddies directed towards the cylinder, meaning that particles need to be trapped in a rotating eddy, following its motion. Which particles are captured on the backside is dependent on the particle response time τ_{p} (equation (2.13)), which is proportional to St.

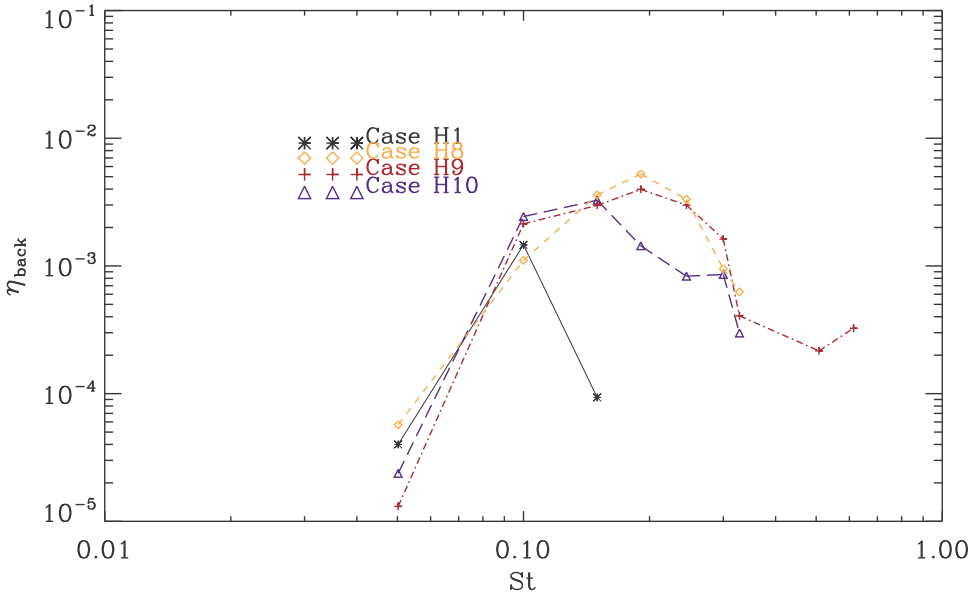

Figure 5.13: Values of the backside capture efficiency in the $\mathrm{Re_c} = 1685$ simulations with turbulent velocity magnitude $\mu_{\mathrm{turb}} = 2.0$.

Table 5.3: Approximate values of the backside capture efficiency for $\mathrm{Re_c} = 1685$ simulations. As clear differences are found between the $\mu_{\mathrm{turb}} = 1.0$ and $\mu_{\mathrm{turb}} = 2.0$ simulations, only these are given, together with the laminar result. The values are given in units of 10^{-4}.

		$\mu_{\mathrm{turb}} = 1.0$			$\mu_{\mathrm{turb}} = 2.0$		
	Laminar	$k_{\mathrm{f}} = 15$	$k_{\mathrm{f}} = 5$	$k_{\mathrm{f}} = 1.5$	$k_{\mathrm{f}} = 15$	$k_{\mathrm{f}} = 5$	$k_{\mathrm{f}} = 1.5$
St	H1	H2	H3	H4	H8	H9	H10
0.05	0.40	0.57	0	0.24	0.57	0.13	0.24
0.10	15	39	24	19	11	32	24
0.15	0.93	80	25	2.4	36	30	33
0.19	0	31	5	0.5	52	39	14
0.245	0	17	0.90	0	33	30	8.3
0.30	0	7.5	0	0	9.5	16	8.6
0.328	0	8.1	0	0	6.2	4.1	3.0
0.51	0	0	0	0	0	2.2	0
0.60	0	0	0	0	0	3.3	0

The mechanisms behind backside capture can be explained as follows. As described by Haugen & Kragset (2010) [4], the characteristic time of the eddies, τ_{eddy}, cannot be much different from τ_{p}: If $\tau_{\text{eddy}} \gg \tau_{\text{p}}$, the eddy turn-over is too slow for the centrifugal 'force' to throw the particle towards the wall. When $\tau_{\text{eddy}} \ll \tau_{\text{p}}$, which is the case for large particles, the particle will not have time to respond to the turn-over and thus not obtain the acceleration needed. Thus, a τ_{eddy} in the order of τ_{p} will result in backside capture. Since the forcing scale $l_{\text{f}} = L_{\text{box}}/k_{\text{f}}$ is a characteristic length for the turbulence, the characteristic eddy time can be defined in the same manner as the characteristic fluid time, given by (2.16), such that

$$\tau_{\text{eddy}} = \frac{l_{\text{f}}}{u_{\text{rms}}} = \frac{L_{\text{box}}}{u_{\text{rms}} k_{\text{f}}}. \tag{5.2}$$

In the laminar cases, τ_{eddy} is given by the dimensions of the cylinder, as backside impaction in the laminar cases is caused only by the rotational motion of the vortices in the wake. These wake vortices also play a role in the turbulent η_{back}, but the differences in the turbulent η_{back} can be explained by (5.2).

The product $u_{\text{rms}}k_{\text{f}}$, values of which are found in table 5.1, determines τ_{eddy} for the different turbulent cases. When $\mu_{\text{turb}} = 2.0$, u_{rms} is doubled, giving an even lower τ_{eddy}. According to these values, one would expect the maximum of η_{back} for $k_{\text{f}} = 15$ to be found for a lower St than in it is for $k_{\text{f}} = 1.5$, as τ_{eddy} is smallest for higher k_{f}. But as seen in table 5.3 or figures 5.12 and 5.13, this is not the case; in the $\mu_{\text{turb}} = 1.0$ case, η_{back} spans across a larger St range for $k_{\text{f}} = 15$ than it does for both $k_{\text{f}} = 5$ and $k_{\text{f}} = 1.5$, and it attains considerably higher values both for $\mu_{\text{turb}} = 1.0$ and $\mu_{\text{turb}} = 2.0$. Therefore, another mechanism must be into play, and this will be discussed in section 5.6.

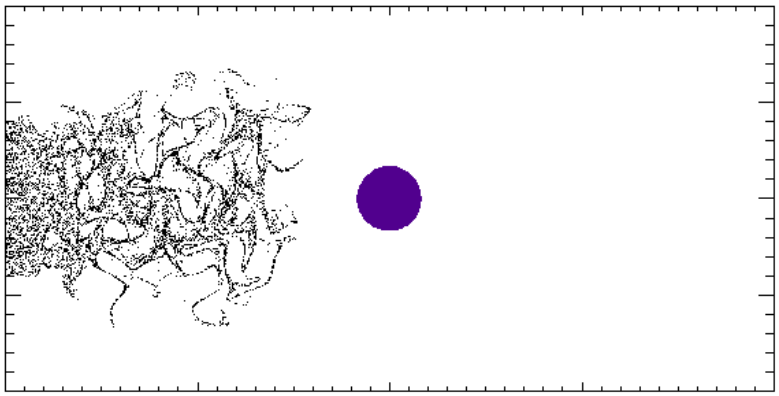

(a) $k_\mathrm{f} = 15$

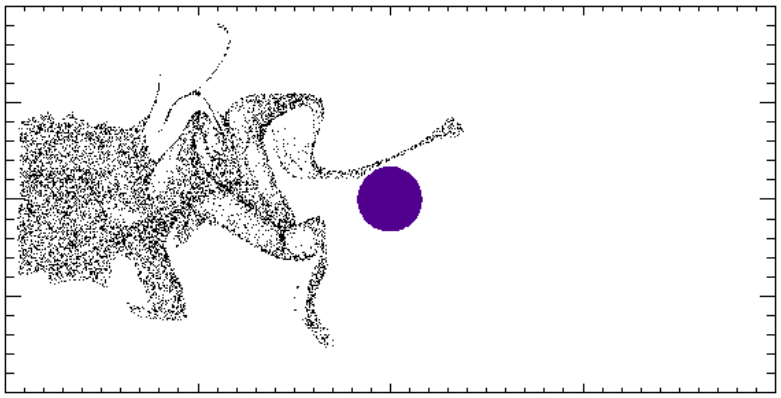

(b) $k_\mathrm{f} = 5$

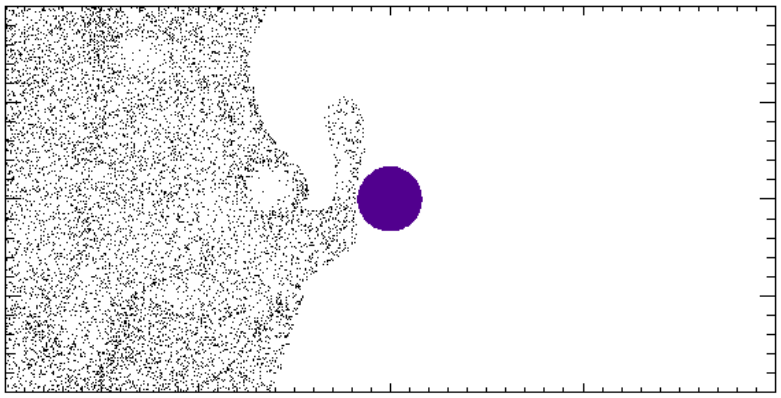

(c) $k_\mathrm{f} = 1.5$

Figure 5.14: Clustering of particles with St = 0.30, turbulent cases with $\mu_\mathrm{turb} = 1.5$ run at $\mathrm{Re_c} = 1685$.

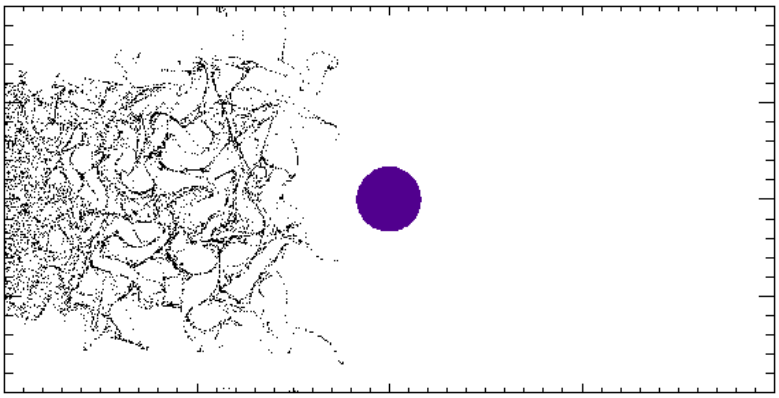

(a) St = 0.30

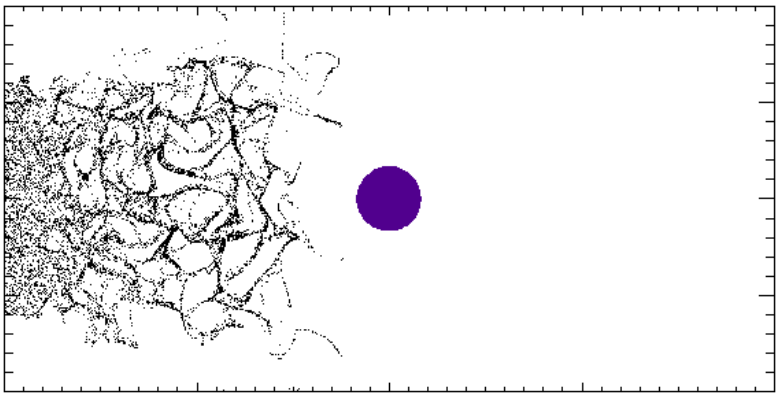

(b) St = 0.76

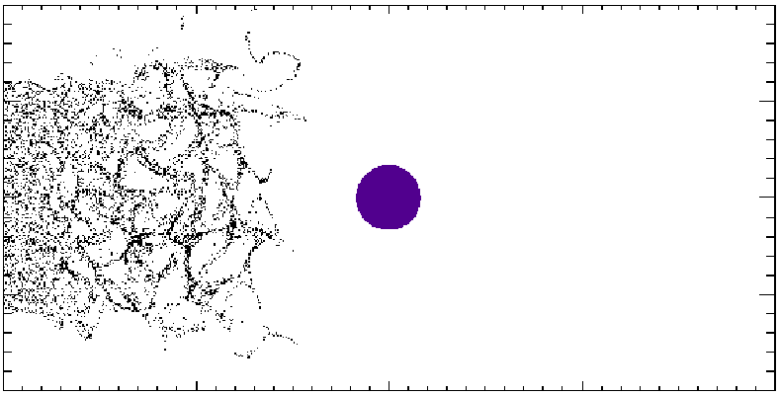

(c) St = 1.2

Figure 5.15: Clustering of particles in turbulence forced at $k_\mathrm{f} = 15$. All cases are run with $\mu_\mathrm{turb} = 2.0$.

5.5 Particle clustering

For $\mathrm{Re_c} = 1685$, the particles exhibited preferential concentration or clustering. The $\mathrm{Re_c} = 421$ cases are not considered, as the phenomenon is less apparent here. The mechanisms behind particle clustering are the same as those behind backside impaction. Continuing the discussion from the previous section, the eddy Stokes number can be introduced as

$$\mathrm{St_{eddy}} = \frac{\tau_\mathrm{p}}{\tau_\mathrm{eddy}} = \frac{\tau_\mathrm{f}}{\tau_\mathrm{eddy}}\mathrm{St}. \tag{5.3}$$

Here, the definition $\mathrm{St} = \tau_\mathrm{p}/\tau_\mathrm{f}$ has been used. With the characteristic fluid time $\tau_\mathrm{f} = D/U_0$ and the characteristic eddy time τ_eddy given by (5.2), equation (5.3) can be expressed as

$$\mathrm{St_{eddy}} = \frac{D}{U_0}\frac{u_\mathrm{rms}k_\mathrm{f}}{L_\mathrm{box}}\mathrm{St}. \tag{5.4}$$

As explained in the previous section, $\tau_\mathrm{p} \sim \tau_\mathrm{eddy}$ is needed for back side deposition, and thus also particle clustering, to take place. Thus, $\mathrm{St_{eddy}} \sim 1$ is needed. As it is $u_\mathrm{rms}k_\mathrm{f}$ in the prefactor in front of St in (5.4) that is varying between the different turbulent cases, this product determines for which Stokes numbers clustering will be large, namely for those implying $\mathrm{St_{eddy}} \sim 1$. For the Stokes numbers considered in this work, this implies that particle clustering is largest at $k_\mathrm{f} = 15$, while the effect gets smaller for decreasing k_f. This can be seen by inserting numerical values into $\mathrm{St_{eddy}}$. The discussion of the role of the vorticity in the next section is related to this explanation, since it is the vorticity of the turbulent eddies that give rise to $\mathrm{St_{eddy}}$, with the magnitude of vorticity $\omega \propto u_\mathrm{rms}k_\mathrm{f}$.

Figure 5.14 shows the scenario when all particles have entered the domain for the three turbulent cases with turbulent magnitude $\mu_\mathrm{turb} = 1.5$, all depicting $\mathrm{St} = 0.3$ particles. The clustering is seen to be largest in 5.14(a), at $k_\mathrm{f} = 15$, resonable as this case has the largest value of $u_\mathrm{rms}k_\mathrm{f}$. In this case, many small eddies with high vorticity lead to accumulation of particles in the shear zones between them. This is to a somewhat less extent also happening in 5.14(b), at $k_\mathrm{f} = 5$. The larger eddies make the particles being dispersed across a larger area, seen for instance by the 'arm of particles' stretching out above the cylinder. But the clustering is less apparent due to the local vorticity being smaller than in 5.14(a). At the largest forcing scale, at $k_\mathrm{f} = 1.5$ in 5.14(c), clustering is even less apparent, but can also here be observed, e.g. around a large eddy just in front of the cylinder.

Figure 5.15 shows clustering for three different particle sizes for a $k_\mathrm{f} = 15$ case run with $\mu_\mathrm{turb} = 2.0$. As the magnitudes of the three St are not very

different from each other, the degree of clustering is roughly equal in all cases. The higher u_{rms}, due to higher μ_{turb}, makes it plausible that the clustering is seen to be higher here than in figure 5.14(a), which was predicted by (5.4). However, the figures are only qualitative verifications that clustering occurs at $\text{Re}_c = 1685$, and that it is related to backside capture. No further conclusions regarding clustering are made in the present work.

5.6 The role of the vorticity

It has been seen that the turbulent eddies, and thus the vorticity containing parts of the flow, have considerable effects on the frontside capture efficiencies. In the figures 5.16 and 5.17, the vorticity component ω_z is plotted for different cases.

The laminar scenarios are depicted in figures 5.16(a) and (b), and show the non-zero vorticity of the vortices in the cylinder wake. A major difference between the $\text{Re}_c = 421$ and the $\text{Re}_c = 1685$ turbulence, is how the vorticity is sustained in the latter case. This reflects the slower dissipation of the lower viscosity ν, cf. 5.16(c) versus (d) and 5.16(e) versus (f). The higher viscosity in $\text{Re}_c = 421$ cases also leads to particle clustering being less apparent than in the $\text{Re}_c = 1685$ cases. Furthermore, the vorticity is larger in the small scale forced cases, cf. 5.16(c) and (d) forced at $k_f = 15$ versus 5.16(e) and (f) forced at $k_f = 5$; the smaller forcing length implies high concentration of eddies, and thus vorticity. This trend is also seen for $\text{Re}_c = 1685$, cf. figures 5.16(d) and (f) and 5.17(a). On the other side, as energy is 'put in' at a smaller scale, the eddies are dissipated faster, as seen by comparing 5.16(c) and (e). This is also expressed by the higher u_{rms} in the latter case. But in the $\text{Re}_c = 1685$ cases, the energy of the eddies is sustained well throughout the domain. The figures 5.17(a) and (d) show the turbulent $k_f = 1.5$ cases with $\mu_{\text{turb}} = 1.0$ and $\mu_{\text{turb}} = 2.0$ respectively. Here, another effect is demonstrated; the increased turbulent velocity in (d), compared to (a), leads to higher vorticity at the inlet and thus also throughout the domain.

These vorticity plots also further explain the increased backside capture efficiencies for higher Re_c. The vorticity downstream of the cylinder is larger in case H2 than in H3 and H4, and leads to higher backside capture efficiency. This is probably why the trend predicted by (5.2) was not fully present in the backside capture results; the effect of the higher vorticity overruns what was predicted about the η_{back} results by the value of $u_{\text{rms}}k_f$ in (5.2), and the vorticity magnitude is thus the driving force behind backside impaction. When $\mu_{\text{turb}} = 2.0$, the differences in vorticity magnitude between the turbulent cases are smaller than when $\mu_{\text{turb}} = 1.0$. This is seen when comparing

the $\mu_{\text{turb}} = 1.0$ figures 5.16(d), (f) and 5.17(a) versus the $\mu_{\text{turb}} = 2.0$ figures 5.17(b), (c) and (d). This higher degree of homogeneity probably leads to the less spreading in the back side capture efficiency for $\mu_{\text{turb}} = 2.0$.

In all cases at both Re_c, the boundary layer seems to have the same structure, also with turbulence imposed; very close to the cylinder, high vorticity concentration is found. This was also observed by Bjørnstad (2010) [11]. This implies that the increased capture for turbulent cases in the boundary stopping mode is not due to the turbulence modifying the boundary layer structure. The boundary layer also need much higher Re_c to become turbulent, cf. section 1.2.4. The next chapter investigates the assumed reason of the higher frontside capture efficiencies when turbulence is present.

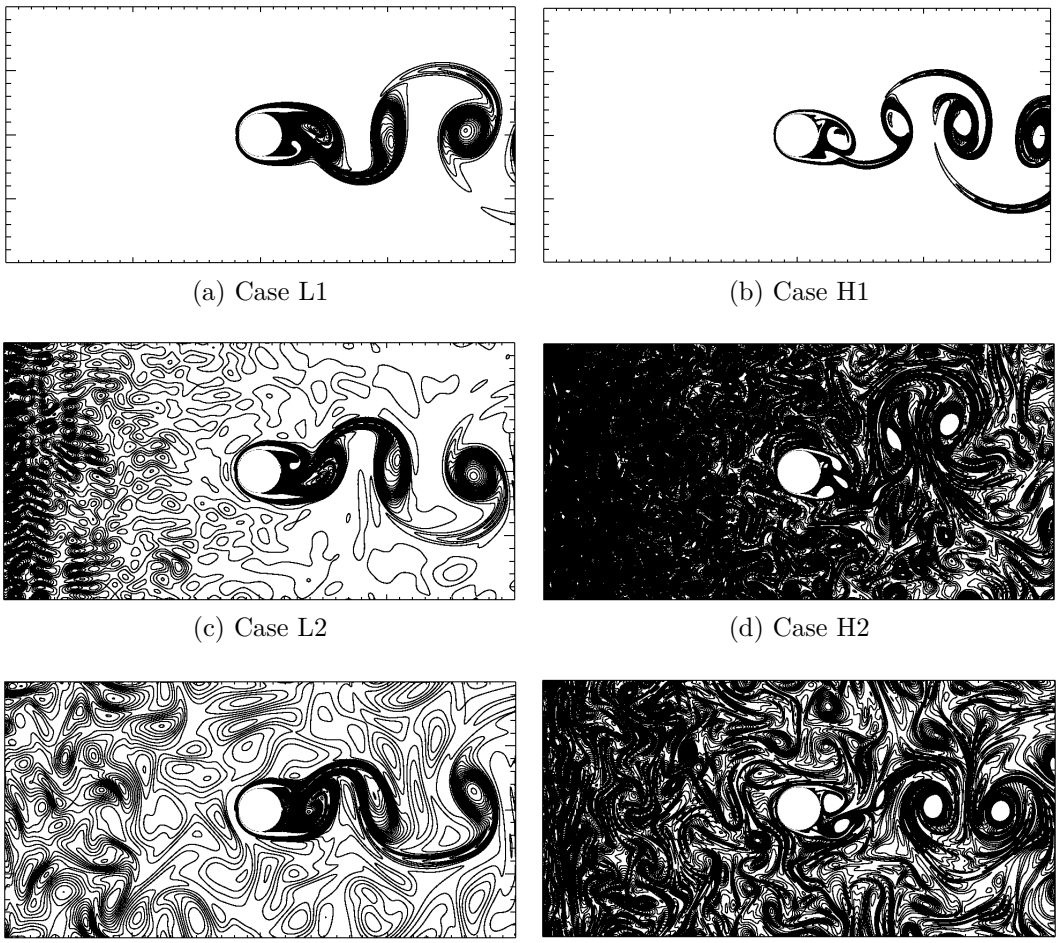

(a) Case L1 (b) Case H1

(c) Case L2 (d) Case H2

(e) Case L3 (f) Case H3

Figure 5.16: Contour plots of the vorticity component ω_z. All figures show the whole 2D domain, with the cylinder coloured white in the center. Regions of highly concentrated vorticity are couloured black. Cases with an 'L' are $\mathrm{Re_c} = 421$ simulations, 'H' indicates $\mathrm{Re_c} = 1685$.

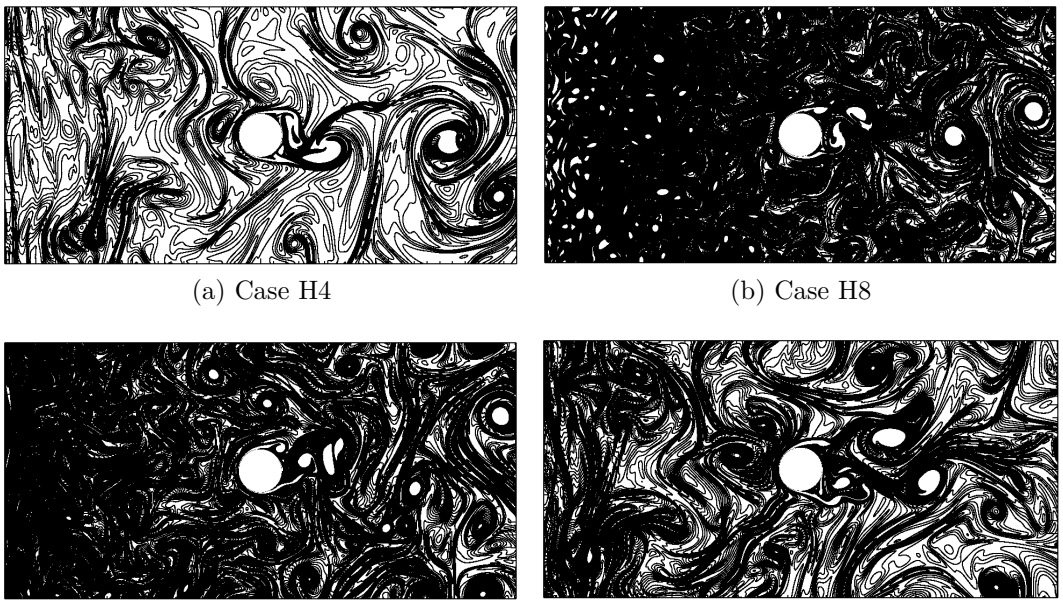

(a) Case H4 (b) Case H8

(c) Case H9 (d) Case H10

Figure 5.17: Contour plots of the vorticity component ω_z for some $\mathrm{Re_c} = 1685$ cases. In (a), turbulence is forced at $k_\mathrm{f} = 1.5$, with $\mu_\mathrm{turb} = 1.0$. The figures (b), (c) and (d) show $\mu_\mathrm{turb} = 2.0$ turbulence with $k_\mathrm{f} = 15$, $k_\mathrm{f} = 5$ and $k_\mathrm{f} = 1.5$ respectively.

Chapter 6

The frontside capture efficiency in turbulent flow

The goal of this chapter is in a quantitative manner to fully explain why the frontside capture efficiencies in the turbulent cases differ from the laminar ones, and theoretically predict the frontside capture efficiencies in the turbulent cases. Throughout the chapter, all capture efficiencies discussed are frontside capture efficiencies.

6.1 The stochastic nature of the Stokes number

The Stokes number St is proportional to the fluid flow velocity, cf. (2.15) and (2.16). In the turbulent case, the magnitude of the fluid flow velocity V, in general different from the mean flow velocity U_0, is stochastically fluctuating. Thus, the Stokes number also is a stochastic variable, effectively being different from the 'laminar' St, expressed by the laminar fluid velocity U_0. This effective Stokes number can then be expressed as

$$\mathrm{St}_{\mathrm{eff}} = \frac{\mathrm{St}}{U_0} V, \tag{6.1}$$

where St is given by (2.15) and (2.16). As $\mathrm{St}_{\mathrm{eff}}$ is a linear function of V, its variance becomes

$$Var(\mathrm{St}_{\mathrm{eff}}) \equiv \sigma^2_{\mathrm{St}} = \left(\frac{\mathrm{St}}{U_0}\right)^2 Var(V), \tag{6.2}$$

cf. Walpole et al., 2007 [35]. Since U_0 has zero variance, (6.2) shows that $\sigma^2_{\mathrm{St}} = 0$ when $V = U_0$. The expectation value of the effective Stokes number equals

$$E(\mathrm{St}_{\mathrm{eff}}) \equiv \mu = \mathrm{St}, \tag{6.3}$$

which is natural since V fluctuates symmetrically around U_0.

With a fluctuation in V_{eff}, the effective Stokes number becomes $\mathrm{St}_{\mathrm{eff}} = \mathrm{St} + \Delta$, with Δ being the resulting fluctuation in the Stokes number. Thus, a Taylor expansion in the small parameter Δ yields, by using (6.3),

$$\begin{aligned} \eta(\mathrm{St}_{\mathrm{eff}}) &= \eta(\mathrm{St} + \Delta)] \\ &= \eta(\mu) + \eta'(\mu)\Delta + \frac{\eta''(\mu)}{2}\Delta^2 + \mathcal{O}(\Delta^3). \end{aligned} \tag{6.4}$$

The expectation value of this becomes

$$\begin{aligned} E[\eta(\mathrm{St}_{\mathrm{eff}})] &= \eta(\mu) + \eta'(\mu)E[\Delta] + \frac{\eta''(\mu)}{2}E[\Delta^2] + \mathcal{O}(E[\Delta^3]) \\ &\approx \eta(\mu) + \frac{\eta''(\mu)}{2}\sigma^2_{\mathrm{St}}. \end{aligned} \tag{6.5}$$

By definition, $\sigma^2_{\mathrm{St}} \equiv E[\Delta^2] - (E[\Delta])^2 = E[\Delta^2]$. Here, it is used that $E[\Delta] = 0$, due to the symmetry of the velocity fluctuations around the mean. Furthermore, higher order terms, $\mathcal{O}(E[\Delta^3])$, have been neglected. The definition of μ in (6.3) implies that $\eta(\mu)$ is the laminar capture efficiency. In order to use (6.5) to obtain the expected values of the frontside capture efficiencies with turbulence present, values for $\eta''(\mu)$ are found. The results are discussed in the next section.

Furthermore, σ^2_{St} is needed to determine the frontside capture efficiency $\eta(\mathrm{St}_{\mathrm{eff}})$ for a given St. This can be found from the turbulent simulation results, by looking at how the velocity of the particles deviate from the mean flow velocity U_0. This deviation expresses how the turbulence affects the particles, and will typically be different for different Stokes numbers. This gives each Stokes number a unique σ^2_{St}. According to Walpole et al. (2007) [35] it is appropriate to use the *sample variance*,

$$S^2_{V,\mathrm{St}} = \frac{1}{n-1}\sum_{(p,\mathrm{St})=1}^{n}(V_{p,\mathrm{St}} - U_0)^2, \tag{6.6}$$

as an estimate of $Var(V)$. Here, the deviations from U_0 of all the respective particle velocities of all n particles of a given St are summed. The positions and velocities of all particles are available at several time instants, and can be returned from the code. Values of $V_{p,\mathrm{St}}$ were found in the different turbulent

simulations by looking at the velocities of all particles of each Stokes number at all y-positions within an appropriate x range $\Delta x_{p,\mathrm{St}}$. To find reliable values, the particles should not be too close to the cylinder, which is centered at $x = 0.2$; they should only be affected by the turbulent eddies, not the geometry of the cylinder. For the turbulence to have time to fully act on the particle motion, $x_{p,\mathrm{St}}$ should on the other side not be too close to $x = 0$. For the calculations here, the range $\Delta x_{p,\mathrm{St}} \in [0.08, 0.12]$ was chosen, rather arbitratily, since approximately the same values of $S^2_{V,\mathrm{St}}$ were attained as long as $x_{p,\mathrm{St}}$ fulfilled the constraints indicated above.

The variance σ^2_{St} of the effective Stokes number, according to (6.2) and with $Var(V) = S^2_V$, was calculated for the $\mu_{\mathrm{turb}} = 1.0$ turbulent cases L2-L4 and H2-H4. The values are given in table 6.1. The values of σ^2_{St} increase dramatically as St increases, for all turbulent forcing scales. Also, a larger forcing scale gives larger σ^2_{St}, which is natural since larger turbulent eddies imply larger σ^2_{St}. The effect of the Reynolds number is also clear; the turbulent eddies influence the particles more in the highest $\mathrm{Re_c}$ cases. This is due to the lower degree of viscous dissipation. However, at the $k_{\mathrm{f}} = 1.5$ case at $\mathrm{Re_c} = 421$, all particles have larger σ^2_{St} than the corresponding case at $\mathrm{Re_c} = 1685$. This is related to the high steady state u_{rms} of the $k_{\mathrm{f}} = 1.5$ turbulence at $\mathrm{Re_c} = 421$, cf. table 5.1.

Also, the differences in σ^2_{St} between the $\mathrm{Re_c} = 421$ cases are larger than it is between the $\mathrm{Re_c} = 1685$ cases. In the latter cases, the $k_{\mathrm{f}} = 5$ simulation has even higher σ^2_{St} than the $k_{\mathrm{f}} = 1.5$ run for all St, except for $\mathrm{St} = 10.0$. Thus, the values of σ^2_{St} becomes less dependent on k_{f} as the Reynolds number increases. This indicates that there probably exists some Reynolds number for which σ^2_{St} converges towards a maximum for all k_{f}.

As earlier explained, the smaller a particle is, the more it is influenced by the turbulent velocity fluctuations; so particles with small Stokes numbers have larger $Var(V)$ than particles with large Stokes numbers, a fact verified by the calculated values of S^2_V. But as the values in the upper Stokes number range are much larger than those in the lower, the value of the Stokes numbers becomes dominating in the calculation of σ^2_{St}, cf. (6.2). Therefore, σ^2_{St} becomes larger as St increases, as is seen in table 6.1.

6.2 Fitting the η curves for laminar flow

In the model for the expectation value $E[\eta(\mathrm{St_{eff}})]$ in (6.5), a twice differentiable expression $\eta(\mu)$ for the laminar capture efficiency is needed. The shapes of the respective curves for case L1 in figure 5.3 and case H1 in figure 5.5 are seen to resemble *sigmoidal growth curves* (Seber & Wild, 1989 [36]).

Table 6.1: The variance σ^2_{St} of all St, calculated from the turbulent simulation results. The values are given in units of 10^{-4}. The forcing wavenumber $k_\mathrm{f} = 15$ corresponds to cases L2 and H2, $k_\mathrm{f} = 5$ to L3 and H3 and the large scale forcing $k_\mathrm{f} = 1.5$ to cases L4 and H4.

	$\mathrm{Re_c} = 421$			$\mathrm{Re_c} = 1685$		
St	$k_\mathrm{f} = 15$	$k_\mathrm{f} = 5$	$k_\mathrm{f} = 1.5$	$k_\mathrm{f} = 15$	$k_\mathrm{f} = 5$	$k_\mathrm{f} = 1.5$
0.05	0.114	0.268	1.2	0.434	0.557	0.515
0.10	0.424	1.07	4.72	1.67	2.18	2.03
0.15	0.891	2.34	10.5	3.56	4.88	4.6
0.19	1.37	3.84	17.4	5.57	7.94	7.29
0.245	2.11	6.11	28.9	8.89	12.7	12.4
0.30	3.10	9.18	50.9	12.3	18.6	17.9
0.328	3.48	11.1	50.9	14.5	22.7	21.2
0.51	8.0	24.2	120	30.9	52.9	50.4
0.60	10.57	36.1	166	42.7	73.7	71.1
1.0	29.1	75.4	424	96.4	157	178
3.0	188.4	452	2615	597	1203	1185
10.0	689	2539	10205	3444	4372	6321

By using this knowledge and further analyzing the characteristics of the laminar curves in figure 5.9(a), analytical expressions for $\eta(\mu)$ in the respective laminar cases are found by nonlinear regressions. Details on the procedure can be found in appendix A.1, and the resulting curves are plotted in figure 6.1. The second derivative $\eta''(\mu)$ evaluated in all twelve laminar η data points is the quantity of interest, and is plotted in figure 6.2: The second derivative plotted in 6.2(a) is very close to zero for $\mathrm{St} < 0.19$ and $\mathrm{St} \gtrsim 0.5$, while in (b), $\eta''(\mu) \approx 0$ for $\mathrm{St} < 0.19$ and $\mathrm{St} \gtrsim 1.0$. But in the latter case, $\eta''(\mu)$ is negative but close to zero for $\mathrm{St} \gtrsim 0.50$. Thus, $0.19 \lesssim \mathrm{St} \lesssim 0.50$ is the range where the predicted frontside capture efficiency for the turbulent cases will be considerably different than the laminar, according to (6.5). This St range coincides well with the boundary stopping mode described in chapter 5.

The values of $\eta''(\mu)$, plotted in figure 6.2, are in the range $0.19 \lesssim \mathrm{St} \lesssim 0.35$ considerably higher than the values of σ^2_{St} in this range. This means the calculated $\eta(\mathrm{St_{eff}})$, according to (6.5) will be very sensitive do the value of $\eta''(\mu)$. In order to find satisfactorily accurate values for $\eta''(\mu)$ in this range, a new regression procedure was done to better match the $\mathrm{Re_c} = 421$ data here, while $\eta''(\mu)$ was found numerically for the $\mathrm{Re_c} = 1685$ data, as it proved difficult to find a more accurate regression curve, than the one shown in figure

6.1(b). The procedure is explained in appendix A.2, where also the values of $\eta''(\mu)$ are listed.

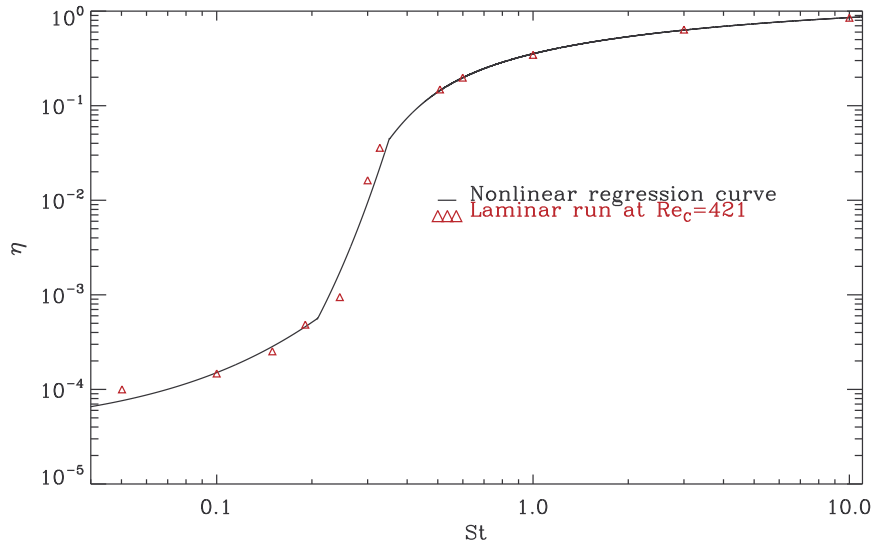

(a)

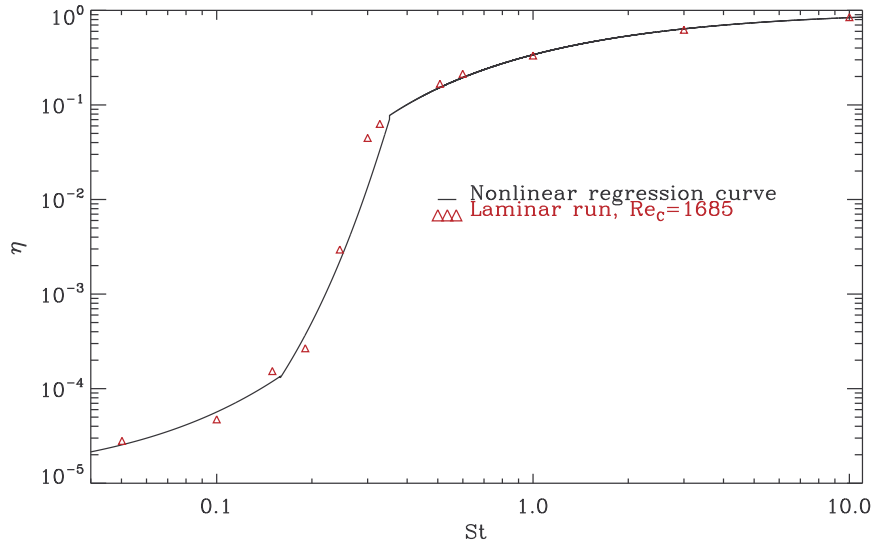

(b)

Figure 6.1: The laminar capture efficiency data is plotted versus St, with the regression curve $\eta(\mathrm{St}) = \eta(\mu)$, at $\mathrm{Re_c} = 421$ in (a) and $\mathrm{Re_c} = 1685$ in (b).

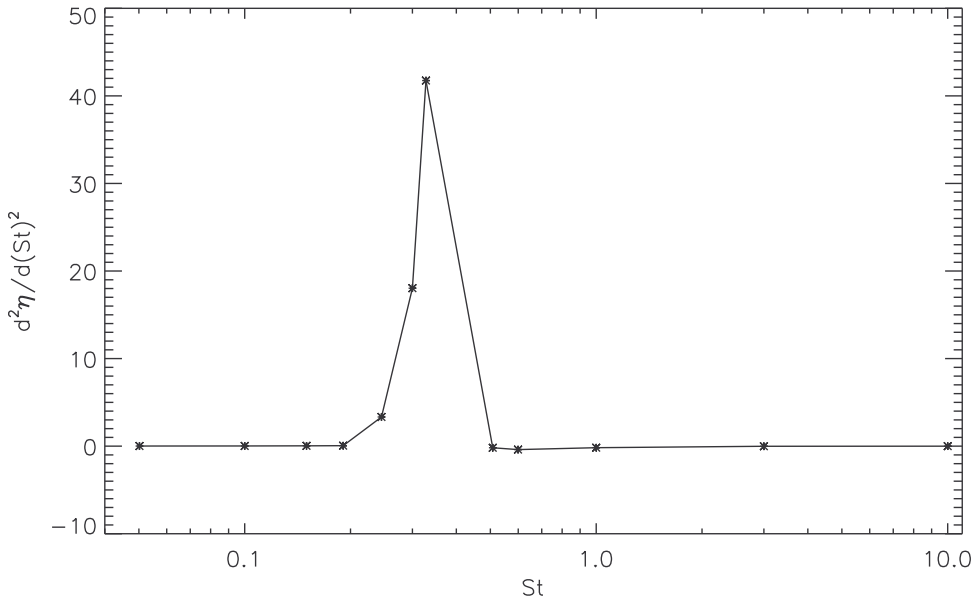

(a)

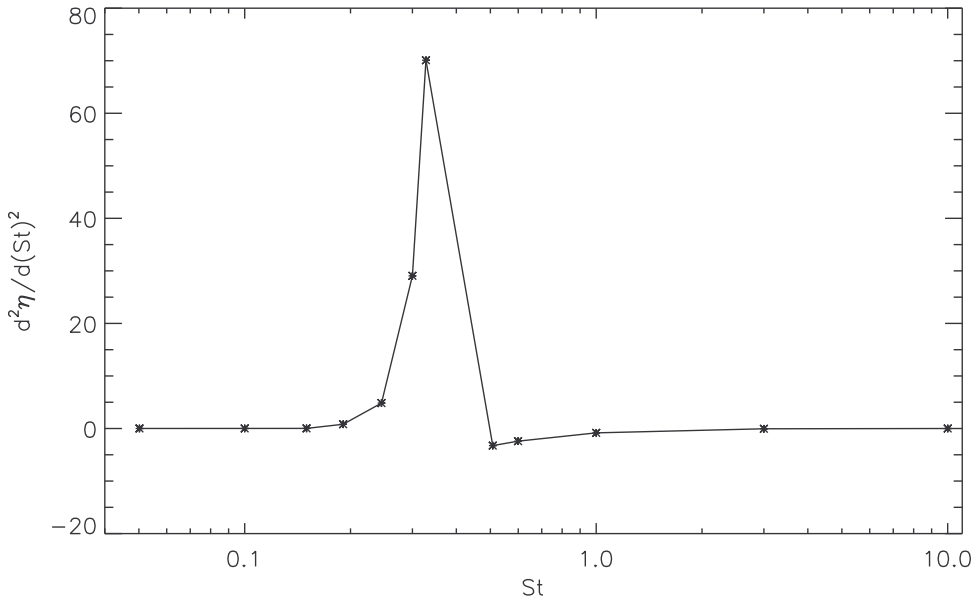

(b)

Figure 6.2: The second derivative of the curves $\eta(\mathrm{St}) = \eta(\mu)$ fitted to the laminar η data, in (a) at $\mathrm{Re_c} = 421$ and in (b) at $\mathrm{Re_c} = 1685$.

6.3 Predicting the η values in the cases with turbulence

Values of σ_{St}^2 were inserted into (6.5) together with the laminar capture efficiencies $\eta(\mu)$ and their double derivatives $\eta''(\mu)$. This theoretical result should ideally match η from the simulations of the different turbulent cases. The figures 6.3 through 6.5 show the predicted η values together with the simulation results. Only the $\mu_{\mathrm{turb}} = 1.0$ cases have been considered at $\mathrm{Re_c} = 1685$.

In the calculations, $\eta''(\mu)$ has been set to zero at the three lowest St and the five highest St, due to what is seen in figure 6.2 and to the arguments in the previous section. Thus, the calculated $\eta(\mathrm{St_{eff}})$ is equal to $\eta(\mu)$ for all these St. This is, as seen in figures 6.3 - 6.5, legitimate: In the inertial impaction mode, the differences between the calculated $\eta(\mathrm{St_{eff}})$ and the laminar are minimal and due to deviations in the data, caused by the low number of particles here.

At the lowest Stokes numbers, the results of the simulations with turbulence clearly do not match what is predicted by (6.5). Even if $\eta''(\mu) \approx 0$ in this regime, the capture efficiencies from the simulations with turbulence deviate from those from the laminar simulations, and thus also the calculated values. Looking at figure 6.5(b), the $k_{\mathrm{f}} = 1.5$ case at $\mathrm{Re_c} = 1685$, the simulated capture at the two lowest Stokes numbers deviate from the calculated one. As k_{f} is increased, the calculated values of the capture for the lowest Stokes numbers deviate more from the values from the simulations: In the $k_{\mathrm{f}} = 5$ case in figure 6.4, the calculated capture at the four lowest Stokes numbers are wrong compared to the simulation, while in the $k_{\mathrm{f}} = 15$ case, this is the case for the five lowest ones. Another trend is the slightly higher capture for the lowest Stokes number than for the second lowest. This is observed in all $\mathrm{Re_c} = 1685$ cases. Also for $\mathrm{Re_c} = 421$, the capture in the simulations consistently deviates from the calculated value at the three lowest Stokes number.

As a very high number of particles is released in this St range, there is a not negligible number of particles captured, and thus it is not necessarily statistical uncertainties that cause these deviations. The trend seems too clear for the deviations to be random, or due to discrepancies in the data. Conclusively, there might be a mechanism not yet explained in the literature that cause the results in the boundary interception mode to deviate from the predictions in (6.5). If so, this effect becomes more evident for larger k_{f}, i.e. for scaling at smaller length scales. From the figures 6.3(b) and 6.4(b) it is seen that for larger k_{f}, this effect plays a role also in the lower

region of the boundary stopping mode. The capture of particles with these smallest Stokes numbers is dependent on the thickness and characteristics of the boundary layer, and the full investigation of these details is important for the understanding of the small particle capture here (Haugen & Kragset, 2010 [4]). This mechanism could be related to the eddies throwing particles toward the cylinder frontside, in the same fashion as the mechanism causing backside capture and particle clustering in turbulence.

Anyhow, the influence of the turbulent eddies on the paths of the smallest particles close to the cylinder frontside, should be further investigated in future studies.

The present results lead to the conclusion that (6.5), i.e. the fluctuating Stokes number, only partly explains the turbulent frontside capture efficiency differing from the laminar. The matching between calculated and simulated values in the boundary stopping mode, for the four Stokes numbers in the range $0.19 \leq \mathrm{St} \leq 0.328$, gets better for decreasing k_f, as seen especially in the $\mathrm{Re_c} = 1685$ plots in figures 6.3 through 6.5. Furthermore, the degree to which the calculated capture efficiency in the boundary stopping mode corresponds to the turbulent capture efficiency from the simulations, is as previously mentioned highly sensitive to the values of $\eta''(\mu)$ and σ^2_{St}. Thus, the quality of the result is depending on the accuracy of the regression curves and the numerically approximated value of $\eta''(\mu)$.

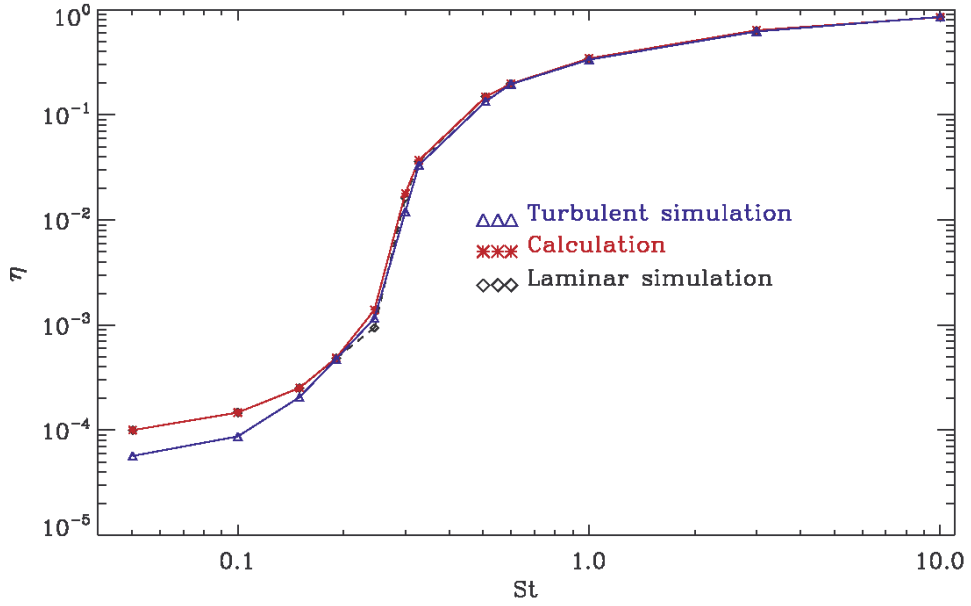

(a) $\mathrm{Re_c} = 421$

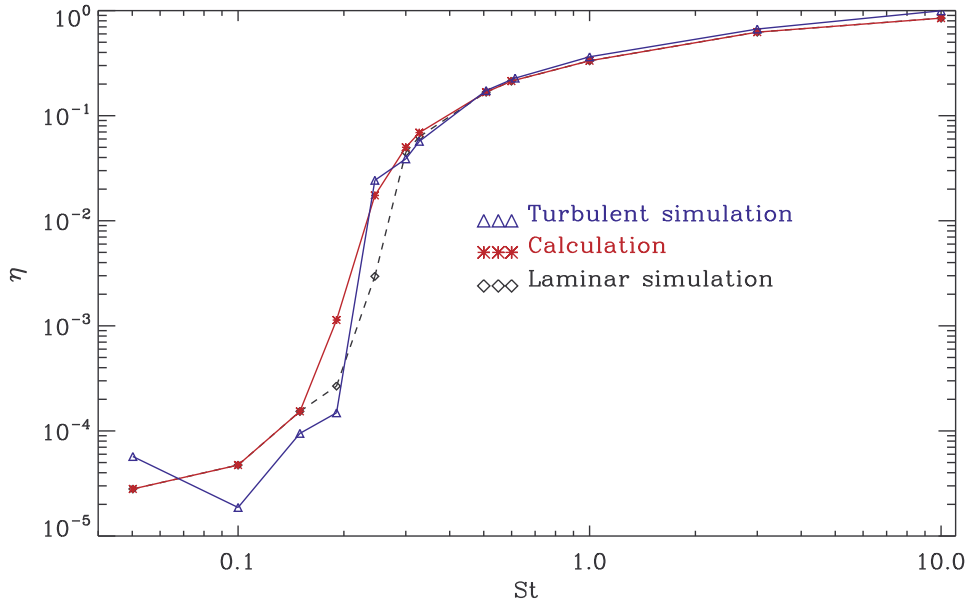

(b) $\mathrm{Re_c} = 1685$

Figure 6.3: Calculated frontside capture efficiency for turbulence at $k_\mathrm{f} = 15$, plotted along with the simulated η, case L2 in (a) and H2 in (b). The laminar results are also plotted for reference.

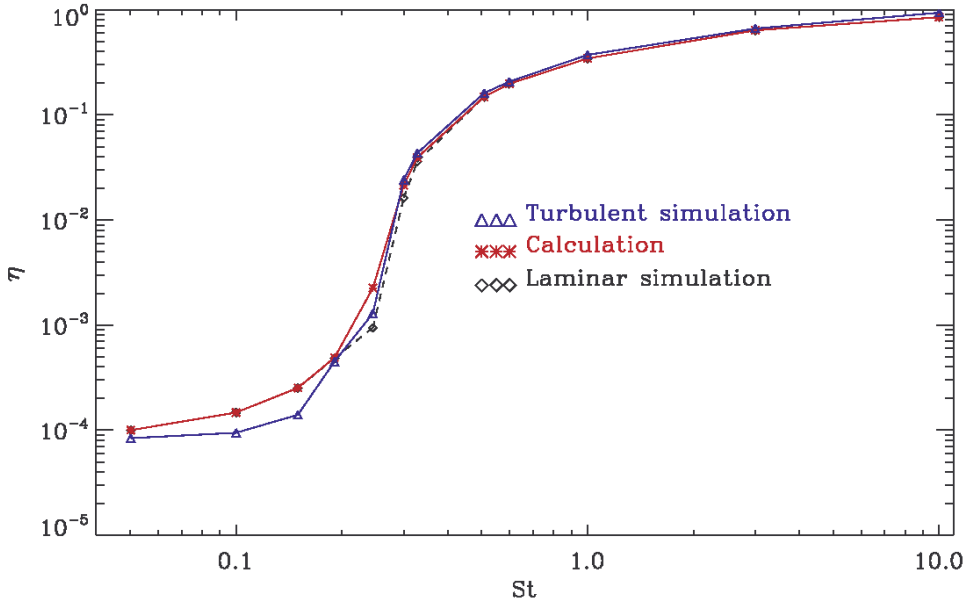

(a) $\mathrm{Re_c} = 421$

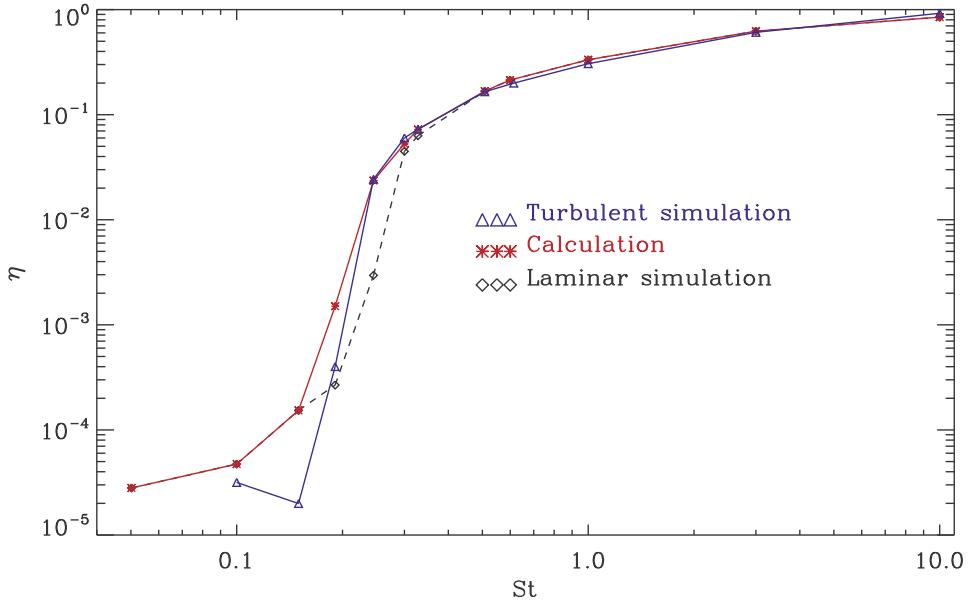

(b) $\mathrm{Re_c} = 1685$

Figure 6.4: Calculated frontside capture efficiency for turbulence at $k_\mathrm{f} = 5$, plotted along with the simulated η at the same forcing wavenumber. Case L3 is seen in (a), case H3 in (b).

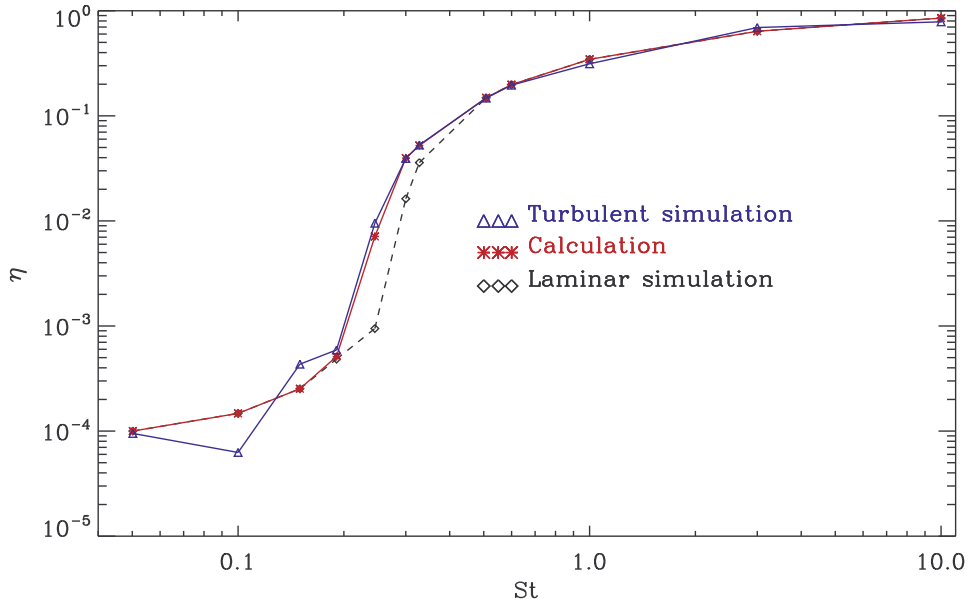

(a) $\mathrm{Re_c} = 421$

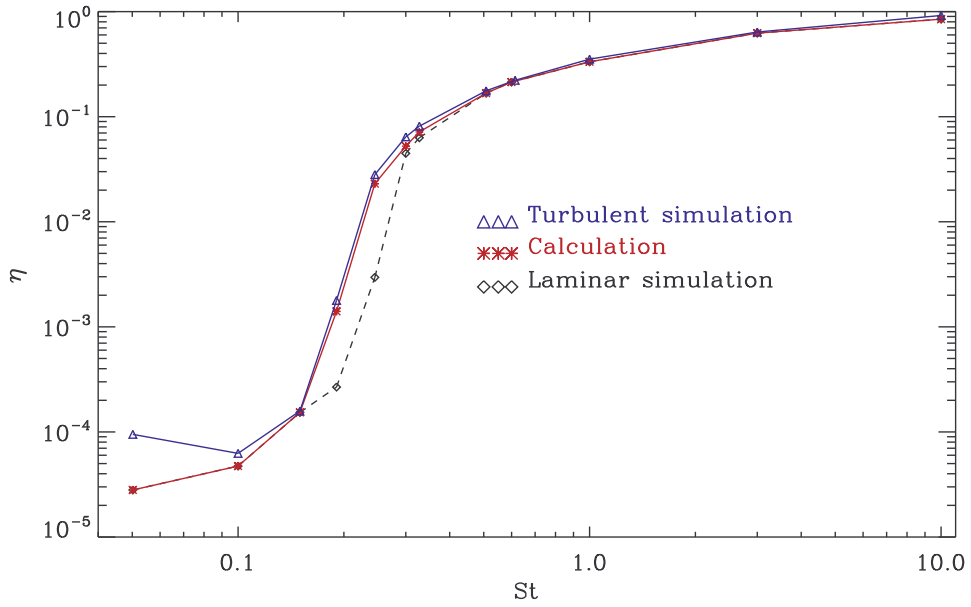

(b) $\mathrm{Re_c} = 1685$

Figure 6.5: Calculated frontside capture efficiency for turbulence at $k_\mathrm{f} = 1.5$, plotted along with the simulated η, in (a) case L4 and in (b) case H4.

Conclusions

By use of Direct Numerical Simulations, the influence of isotropic turbulence on the behaviour of particles and their deposition on a cylinder in a cross flow at two different Reynolds numbers, $\mathrm{Re_c} = 421$ and $\mathrm{Re_c} = 1685$, was studied. Turbulence simulations of varying intensity were run on a three-dimensional domain, with forcing at three different wave numbers. After reaching homogenous steady state, the turbulence was imposed on a two-dimensional flow domain, also with different turbulent velocity magnitudes μ_{turb} increasing the inlet velocity and thus the turbulent fluctuations. Values of $\mu_{\mathrm{turb}} > 2.0$ proved difficult to implement, as this lead to critically large numerical reflections at the boundaries and thus code crash.

The deposition, expressed as the capture efficiency, of particles on the cylinder frontside was seen to be greater in the turbulent cases, compared to laminar reference cases, primarily in the Stokes number range $0.19 \lesssim \mathrm{St} \lesssim 0.328$. This was found to be related to the statistical variance of St, resulting from the fluctuating turbulent velocity leading to fluctuations in the effective Stokes number, as well as the shape of the laminar capture efficiency curve, with the frontside capture increasing rapidly in this Stokes range. As $\mathrm{Re_c}$ was increased from $\mathrm{Re_c} = 421$ to $\mathrm{Re_c} = 1685$, this effect became more dominant, and especially as μ_{turb} was raised. For the smallest particles, in the boundary interception mode, the turbulence also lead to changes in the frontside capture efficiency. However, these changes could not be explained by the fluctuations in the effective Stokes number. This indicates that the turbulence causes some not fully understood mechanism influencing the motion of the smallest particles in the close neighborhood of the boudnary layer of the cylinder. Thus, a closer investigation of this is necessary in further studies.

Particle capture at the backside of the cylinder in the $\mathrm{Re_c} = 1685$ turbulent cases was seen to be relatively large for the lower half of the particle

sizes used. The smaller scale forced turbulence had the largest backside capture for $\mu_{\text{turb}} = 1.0$, due to its vorticity being the largest. The differences in backside capture between the differently forced cases became smaller as μ_{turb} was increased above 1.0. This was due to the resulting increasing vorticity of the flow downstream of the cylinder.

Since the turbulent eddies in the $\text{Re}_{\text{c}} = 1685$ cases were well sustained throughout the two-dimensional domain, the particles dispersed in the turbulent flow exhibited clustering, or preferential concentration. Particle clustering is caused by the same mechanisms as backside impaction. Thus, the magnitude of vorticity, and slow dissipation thereof, is of crucial importance for the clustering to come into play.

Appendices

Appendix A

Obtaining values for $\eta''(\mu)$

In this appendix it is shortly explained how expressions for the laminar capture efficiency $\eta(\mu)$ in both $\mathrm{Re_c}$ cases, and thus values of $\eta''(\mu)$, were obtained.

A.1 Fitting $\eta(\mu)$ for all St

When studying the two laminar capture efficiency curves in figure 5.9(a), one can observe that they resemble a sigmoidal growth nature. A sigmoidal growth function $f(x)$ can be characterized by its growth rate given by

$$\frac{df}{dx} \propto g(f)[h(\alpha) - h(f)], \tag{A.1}$$

where g and h are increasing functions with $g(0) = h(0) = 0$ (Seber & Wild, 1989 [36]). As the simplest model for sigmoidal growth, Seber & Wild (1989) [36] give the *logistic model*

$$f(x) = \frac{\alpha}{1 + e^{-\kappa(\lambda x - \gamma)}}, \quad \text{with } -\infty < x < \infty, \kappa > 0 \text{ and } 0 < f < \alpha, \tag{A.2}$$

which is found by setting $g(f) = h(f) = f$ in (A.1) and the proportionality constant to κ/α. Furthermore, another model is the *Gompertz Growth Curve*

$$f(x) = \alpha \exp(-e^{-\kappa(\lambda x - \gamma)}), \quad \text{with } \kappa > 0 \text{ and } \alpha > 0, \tag{A.3}$$

where g and h have been modified for the growth not to be symmetric about the point of inflection $x = \gamma$, which is where the growth rate df/dx is at its maximum in both (A.2) and (A.3). The shifting parameter $\lambda > 0$ is present in the expressions (A.2) and (A.3) in order to be able to better control the position of the fitting curves.

Table A.1: The approximate values of the curve fitting parameters for $\eta(\mu)$ at $\mathrm{Re_c} = 421$. The result is plotted in 6.1(a).

St range	Equation	α	κ	λ	γ
$\langle 0, 0.208024]$	A.3	1.0	7.5	0.2	0.31
$\langle 0.208024, 0.351886]$	A.2	1.0	31	1.0	0.45

St range	Equation	a	b	c	d	e
$\langle 0.351886, \infty\rangle$	A.5	-0.00121	6.32	0.344	1.47	0.0411

In addition to (A.2) and (A.3), two more sigmoidal fitting equations used are the Janoschek growth function

$$f(x) = \alpha - (1 - \exp(-\kappa x^{\sigma})) \tag{A.4}$$

and a five parameter logistic function

$$f(x)) = d + \frac{a - d}{(1 + (x/c)^b)^e}. \tag{A.5}$$

It proved difficult to fit the laminar η data to a single sigmoidal curve, so a combination of the expressions given above were necessary, with different expressions were used to fit the data for different St ranges, as given in the tables A.1 and A.2. In the equations given, $x = \mathrm{St}$, and the nonlinear regression was done mainly with the programming language Python and its function `curve_fit` from the package `scipy.optimize`*, and also partly with the services provided at the web page *www.zunzun.com*.

Table A.2: The approximate values of the curve fitting parameters for $\eta(\mu)$ at $\mathrm{Re_c} = 1685$. The result is plotted in figure 6.1(b).

St range	Equation	α	κ	λ	γ
$\langle 0, 0.158852]$	A.3	1.0	7.89	0.2	0.309
$\langle 0.158852, 0.351886]$	A.2	1	33	1.0	0.43

St range	Equation	α	κ	σ
$\langle 0.35, \infty\rangle$	A.4	0.99	1.05	-0.81

*Documentation found at *http://docs.scipy.org/doc/scipy/reference/optimize.html*.

A.2 Finding $\eta''(\mu)$ for intermediate St

As the fitted curves seen in figure 6.1, resulting from the procedure explained in the previous section, were found to have $\eta''(\mu) \approx 0$ for $\mathrm{St} < 0.19$ and $\mathrm{St} > 0.328$, a new attempt was made to find functions more accurately fitting $\eta(\mu)$ in both $\mathrm{Re_c}$ cases, valid for $\mathrm{St} \in [0.19, 0.328]$.

In the $\mathrm{Re_c} = 421$ case, the η data points in the range $\mathrm{St} \in [0.19, 0.508]$ were used to fit a function describing $\eta(\mu)$ in this range. The Gompertz growth curve (A.3) was found to match the data nicely with the parameter values given in table A.3.

However, in the $\mathrm{Re_c} = 1685$ case, no satisfactorily accurate curve was found to match the data. As the quantity of interest is $\eta''(\mu)$, this double derivative was found numerically from the η data from the simulation, instead of finding it from a fitted function, as was done in the $\mathrm{Re_c} = 421$ case. This was done by inserting fictive data points near the real data points in the range $\mathrm{St} \in [0.19, 0.328]$, and using the central difference formula for the second derivative, namely

$$f''(x) \approx \frac{f(x - \Delta x) - 2f(x) + f(x + \Delta x)}{(\Delta x)^2}, \tag{A.6}$$

with fictive data points inserted a distance Δx from the original data point, on either side, cf. figure A.1. The values of $\eta''(\mu)$ are given in table A.4.

Table A.3: The approximate values of the curve fitting parameters for $\eta(\mu)$ at $\mathrm{Re_c} = 421$, valid for $\mathrm{St} \in [0.19, 0.508]$.

Equation	α	κ	λ	γ
A.3	0.165	14.9	1	0.356

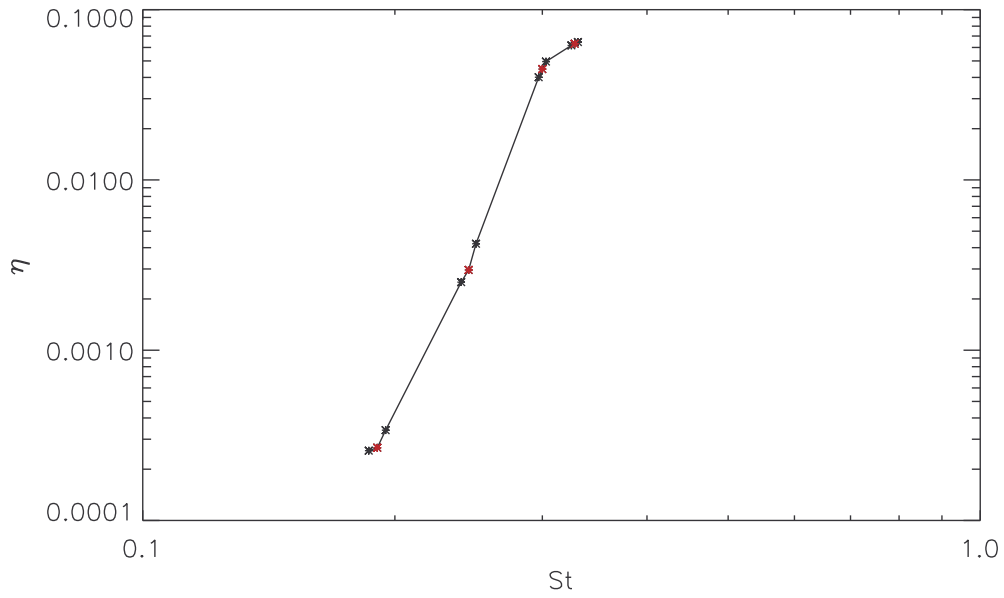

Figure A.1: By inserting fictive data points (black) at either side of the original laminar $\mathrm{Re_c} = 1685$ η data points (red), $\eta''(\mu)$ has been approximated. At the boundaries of the St range, the original η curve has been used as guidance for placing the fictive points.

Table A.4: Values of the second derivatives of the laminar capture efficiency curves, $\eta''(\mu)$, at both Reynolds numbers for intermediate St. These values are used when calculated the expected frontside capture efficiencies $\eta(\mathrm{St_{eff}})$ in (6.5).

St	$\mathrm{Re_c} = 421$	$\mathrm{Re_c} = 1685$
0.19	0.0330137	3.11697
0.24	4.26833	32.5093
0.30	11.0649	8.56507
0.328	6.41324	8.10952

Appendix B

Some parameter values

B.1 Simulations with $\mathrm{Re_c} = 421$

Miscellaneous

Mean free path of gas:	$\lambda = 67 \cdot 10^{-}9$ m
Velocity of mean flow:	$U_0 = 5$ m/s
Kinematic viscosity:	$\nu = 0.0004$ m^2/s, giving $\mathrm{Re_c} = 421.25$
Speed of sound:	$c_\mathrm{s} = 40$ m/s in 2D simulations
	$c_\mathrm{s} = 20$ m/s in 3D simulations

The computational domains

Size of 2D computational domain:	$L_x = 0.4$ m, $L_y = 0.2$ m
Position of the cylinder, center of 2D domain:	$x = 0.2$ m, $y = 0.0$ m
Diameter of cylinder:	$D = 0.0337$ m
Grid points in x and y respectively:	1024×512
Size of 3D computational domain:	$L_\mathrm{box} = 0.2$ m
Grid points in 3D:	$512 \times 512 \times 512$

The particles

Insertion width, laminar case:	$l_{\text{par,lam}} = D$
Insertion width, $k_\text{f} = 15$ forced case:	$l_{\text{par},k_\text{f}=15} \approx 2.35D$
Insertion width, $k_\text{f} = 5$ forced case:	$l_{\text{par},k_\text{f}=5} = 3D$
Insertion width, $k_\text{f} = 1.5$ forced case:	$l_{\text{par},k_\text{f}=1.5} \approx 5.94D$
Total number of particles at each run:	$N = 10^6$
Particle radii given in micrometers:	17.42, 24.63
	30.16, 34
	38.55, 42.66
	44.60, 55.5
	61.03, 77.89
	134.9, 246.3
Stokes numbers:	0.050, 0.10,
	0.15, 0.19,
	0.245, 0.30,
	0.328, 0.508,
	0.614, 1.00,
	3.00, 10.00
Initial velocity of particles:	$v_0 = 5.0$ m/s directed in $\hat{\boldsymbol{x}}$
Particle insertion rate in:	$r_{\text{insert}} = 3.325 \cdot 10^6$ particles/s

B.2 Simulations with $\text{Re}_\text{c} = 1685$

Miscellaneous

Mean free path of gas:	$\lambda = 67 \cdot 10^{-}9$ m
Velocity of mean flow:	$U_0 = 5$ m/s
Kinematic viscosity:	$\nu = 0.0001$ m^2/s, giving $\text{Re}_\text{c} = 1685$
Speed of sound:	$c_\text{s} = 40$ m/s in 2D simulations
	$c_\text{s} = 20$ m/s in 3D simulations

The computational domains

Size of 2D computational domain:	$L_x = 0.4$ m, $L_y = 0.2$ m
Position of the cylinder, center of 2D domain:	$x = 0.2$ m, $y = 0.0$ m
Diameter of cylinder:	$D = 0.0337$ m
Grid points in x and y respectively:	2048×1024
Size of 3D computational domain:	$L_\text{box} = 0.2$ m
Grid points in 3D:	$1024 \times 1024 \times 1024$

The particles

Insertion width, laminar case:	$l_{\mathrm{par,lam}} = D$
Insertion width, $k_\mathrm{f} = 15$ forced cases:	$l_{\mathrm{par},k_\mathrm{f}=15} \approx 3.56D$
Insertion width, $k_\mathrm{f} = 5$ forced cases:	$l_{\mathrm{par},k_\mathrm{f}=5} = 3D$
Insertion width, $k_\mathrm{f} = 1.5$ forced cases:	$l_{\mathrm{par},k_\mathrm{f}=1.5} \approx 5.94D$
Total number of particles at each run:	$N = 10^6$
Particle radii given in micrometers:	8.725, 12.315 15.08, 17 19.275, 21.33 22.30, 27.75 30.515, 38.945 67.45, 123.15
Stokes numbers:	0.050, 0.10, 0.15, 0.19, 0.245, 0.30, 0.328, 0.508, 0.614, 1.00, 3.00, 10.00
Initial velocity of particles:	$v_0 = 5.0$ m/s directed in $\hat{\boldsymbol{x}}$
Particle insertion rate in:	$r_{\mathrm{insert}} = 3.325 \cdot 10^6$ particles/s

Bibliography

[1] M. Boivin, O. Simonin & K. D. Squires (1998). Direct numerical simulation of turbulence modulation by particles in isotropic turbulence, *Journal of Fluid Mechanics* **375**, 235-263

[2] C. Crowe, M. Sommerfield & Y. Tsuji (1998). *Multiphase Flows with Droplets and Particles*, CRC Press

[3] C. Pozrikidis (2001). *Fluid Dynamics. Theory, Computation and Numerical Simulation*, Kluwer Academic Publishers

[4] N. E. Haugen & S. Kragset (2010). Particle impaction on a cylinder in a crossflow as function of Stokes and Reynolds numbers, *J. Fluid Mechanics* **661**, 239-261

[5] Brennen, C. (2005). *Fundamentals of Multiphase Flows*, Cambridge University Press

[6] Y. Xu & S. Subramaniam (2010). Effect of particle clusters on carrier flow turbulence: A direct numerical simulation study, *Flow, Turbulence and Combustion* **85**, 735-761

[7] A. Guha (2008). Transport and Deposition of Particles in Turbulent and Laminar Flow, *Annu. Rev. Fluid Mech.* **40**, 311-341

[8] P. L. Douglas & S. Ilias (1988). On the deposition of aerosol particles on cylinders in turbulent cross flow, *Journal of Aerosol Science* **19** (4), 451-462

[9] C. Marchioli, A. Giusti, M. V. Salvetti & A. Soldati (2003). Direct numerical simulation of particle wall transfer and deposition in upward turbulent pipe flow, *International Journal of Multiphase Flow* **29**, 1017-1038

[10] K. Luo, J. R. Fan & K. F. Cen (2006). DNS of particle dispersion and material erosion in gas-solid two-phase circular cylinder wakes, *Proceedings of ASME Fluids Engineering Division Summer Meeting 2006, FEDSM2006* Volume 1 SYMPOSIA, 2006, 573-580

[11] A. G. Bjørnstad (2010). Particle deposition on a cylinder in a turbulent cross flow, Master's thesis, NTNU

[12] L. Talbot, R. K. Cheng, R. W. Schefer & D. R. Willis (1980). Thermophoresis of particles in a heated boundary layer, *J. Fluid Mech.* **101** (pt 4), 737-758

[13] K. D. Squires & J. K. Eaton (1990). Particle response and turbulence modification in isotropic turbulence, *Phys. Fluids* A **2** (7), 1191-1203

[14] S.B. Pope (2000). *Turbulent Flows*, Cambridge University Press

[15] J. Chun, D. L. Koch, S. L. Rani, A. Ahluwalia % L. R. Collins (2005). Clustering of aerosol particles in isotropic turbulence, *J. Fluid Mech.* **536**, 219-251

[16] K. D. Squires & J. K. Eaton (1991). Preferential concentration of particles by turbulence, *Phys. Fluids* A **3** (5)

[17] J. P. L. C. Salazar, J. De Jong, L. Cao, S. H. Woodward, H. Meng & L. R. Collins (2008). Experimental and numerical investigation of inertial particle clustering in isotropic turbulence, *J. Fluid Mech.* **600**, 245-256

[18] A. Aliseda, A. Cartellier, F. Hainaux & J. C. Lasheras (2002). Effect of preferential concentration on the settling velocity of heavy particles in homogeneous isotropic turbulence, *J. Fluid Mech.* **468**, 77-105

[19] A. M. Wood, W. Hwang & J. K. Eaton (2005). Preferential concentration of particles in homogeneous and isotropic turbulence, *International Journal of Multiphase Flow* **31**, 1220-1230

[20] L. P. Wang & M. R. Maxey (1993). Settling velocity and concentration distribution of heavy particles in homogeneous isotropic turbulence, *J. Fluid Mech.* **256**, 27-68

[21] K. -C. Chang, U. -K. Hsu & Y. -C. Kuo (2011). Numerical studies of the turbulent planar mixing layer using nonlinear $k - \epsilon$ model, *Journal of Aeronautics, Astronautics and Aviation, Series B* **43** (1), 43-54

[22] Y. Kaneda, T. Ishihara, M. Yokokawa, K. Itakura & A. Uno (2003). Energy dissipation rate and energy spectrum in high resolution direct numerical simulations of turbulence in a periodic box, *Physics of Fluids* **15** (2), L21-L24

[23] H. K. Versteeg & W. Malalasekera (2007). *An Introduction to Computational Fluid Dynamics. The Finite Volume Method*, Pearson Education Limited

[24] P. Moin & K. Mahesh (1998). Direct Numerical Simulation: A Tool in Turbulence Research, *Annu. Rev. Fluid Mech.* **30**, 539-578

[25] W. Dobler & A. Brandenburg (2010). *The Pencil Code: A High-Order MPI code for MHD Turbulence*.
http://www.nordita.org/software/pencil-code/doc/manual.pdf

[26] J. O. Hinze (1975). *Turbulence*, Second edition, McGraw-Hill Inc.

[27] V. Eswaran & S. B. Pope (1988). An examination of forcing in direct numerical simulations of turbulence, *Computers & Fluids* **16** (3), 257-278

[28] N. E. L. Haugen, A. Brandenburg & W. Dobler (2004). Simulations of nonhelical hydromagnetic turbulence, *Physical Review* E **70**, 016308

[29] T. J. Poinsot & S. K. Lele (1992). Boundary Conditions for Direct Simulations of Compressible Viscous Flows, *Journal of Computational Physics* **101**, 104-129

[30] G. Lodato, P. Domingo & L. Vervisch (2008). Three-dimensional boundary conditions for direct and large-eddy simulation of compressible viscous flows, *Journal of Computational Physics* **227**, 5105-5143

[31] M. R. Maxey, B. K. Patel, E. J. Chang & L. -P. Wang (1997). Simulations of dispersed turbulent multiphase flow, *Fluid Dynamics Research* **20**, 143-156

[32] H. C. Strutt, S. W. Tullis, M. F. Lightstone (2011). Numerical methods for particle-laden DNS of homogeneous isotropic turbulence, *Computers & Fluids* **40**, 210-220

[33] H. C. Wang (1986). Theoretical adhesion efficiency for particles impacting a cylinder at high reynolds number, *Journal of Aerosol Science* **17** (5), 827-837

[34] D. E. Rosner & P. Tandon (1995). Rational prediction of inertially induced particle deposition rates for a cylindrical target in a dust-laden stream, *Chemical Engineering Science* **50**, (21), 3409-3431

[35] R. E. Walpole, R. H. Myers, S. L. Myers & K. Ye (2007). *Probability & Statistics for Engineers & Scientists*, 8th edition, Pearson Prentice Hall

[36] G. A. F. Seber & C. J. Wild (1989). *Nonlinear Regression*, John Wiley & Sons, Inc.